The diurnal dynamics of Gross Primary Productivity using observations from the Advanced Baseline Imager on the Geostationary Operational Environmental Satellites-R Series at an oak savanna ecosystem

A. M. Khan[1], P. C. Stoy[1,2], J. Joiner[3], D. Baldocchi[4], J. Verfaillie[4], M. Chen[5], J. A. Otkin[6]

[1]Nelson Institute for Environmental Studies, University of Wisconsin – Madison, Madison, WI 53706, USA

[2]Department of Biological Systems Engineering, University of Wisconsin – Madison, Madison, WI 53706, USA

[3]National Aeronautics and Space Administration (NASA) Goddard Space Flight Center (GSFC), Greenbelt, MD, USA

[4]Ecosystem Science Division, Department of Environmental Science, Policy and Management, University of California at Berkeley, Berkeley, CA 94720, USA

[5]Department of Forest and Wildlife Ecology, University of Wisconsin-Madison, Madison, WI 53706, USA

[6]Space Science and Engineering Center, Cooperative Institute for Meteorological Satellite Studies, University of Wisconin-Madison, Madison, WI, 53706, USA

Key Points:

- The Geostationary Operational Environmental Satellites-R Series can estimate gross primary productivity every half hour.
- A light response curve provides the best agreement with gross primary productivity estimated at an Ameriflux oak savanna site.
- Diurnal satellite-based estimates of gross primary productivity follow the shift towards the mornings during the dry summers at the site.

Corresponding author: Anam M. Khan, `amkhan7@wisc.edu`

Abstract

Gross Primary Productivity (GPP) is the largest flux in the global carbon cycle and satellite-based GPP estimates have long been used to study the trends and inter-annual variability of GPP. With recent updates to geostationary satellites, we can now explore the diurnal variability of GPP at a comparable spatial resolution to polar-orbiting satellites and at temporal frequencies comparable to eddy covariance (EC) tower sites. We used observations from the Advanced Baseline Imager on the Geostationary Operational Environmental Satellites - R series (GOES-R) to test the ability of sub-daily satellite data to capture the shifts in the diurnal course of GPP at an oak savanna EC site in California, USA that is subject to seasonal soil moisture declines. We optimized parameters for three models to estimate GPP. A light response curve (LRC) achieved the lowest test mean absolute error for winter (1.82 $\mu mol\,CO_2\,m^{-2}\,s^{-1}$), spring (2.51 $\mu mol\,CO_2\,m^{-2}\,s^{-1}$), summer (1.45 $\mu mol\,CO_2\,m^{-2}\,s^{-1}$), and fall (1.25 $\mu mol\,CO_2\,m^{-2}\,s^{-1}$). The ecosystem experienced the largest shift in daily peak GPP in relation to the peak of incoming solar radiation towards the morning hours during the dry summers. The LRC and the light-use efficiency model were in agreement with these patterns of increasing shift of GPP towards the morning hours during the summer months. Our results can help develop diurnal estimates of GPP from geostationary satellites that are sensitive to fluctuating environmental conditions during the day.

Plain Language Summary

Gross Primary Productivity (GPP) quantifies the draw down of atmospheric CO_2 through ecosystem scale photosynthesis. Large scale estimates of GPP are a crucial component of carbon cycle science and can be estimated using satellites. Motivated by the recent advances in the spectral coverage and spatial resolution of geostationary ("weather") satellites, we demonstrate how the Advanced Baseline Imager (ABI) on the Geostationary Operational Environmental Satellites - R series can provide satellite-based, half-hourly GPP estimates at the Tonzi Ranch Ameriflux eddy covariance site in California, USA. We found that a light response curve is able to achieve the best agreement between ABI-based estimates of GPP and GPP partitioned from gas exchange measurements at the eddy covariance site. Previous research has demonstrated that the diurnal peak of GPP shifts increasingly towards the morning at Tonzi Ranch as the year progresses into the dry season. We found that ABI can capture this characteristic seasonal shift of peak diurnal GPP which highlights its ability to measure ecosystem dynamics in addition to the weather patterns that help cause them.

1 Introduction

Gross primary productivity (GPP) is a critical flux in the global carbon cycle because it represents the CO_2 that is drawn down from the atmosphere by ecosystems through gross photosynthesis. Remotely-sensed observations of the Earth have provided critical inputs for global carbon cycle studies and model inter-comparisons, and have revolutionized our understanding of the carbon cycle (Anav et al., 2015; M. Chen et al., 2017; Cramer et al., 1999; Field et al., 1995; Jung et al., 2020; Keenan et al., 2012; O'Sullivan et al., 2020; Prince & Goward, 1995; Ruimy et al., 1996; Running et al., 2004; Xiao et al., 2019; Zhang et al., 2016; Zscheischler et al., 2014). The diurnal to inter-annual variability of GPP is determined by limiting resources, climate, weather conditions, disturbance, phenology, and extreme events (Beer et al., 2010; Gu et al., 2002; Kannenberg et al., 2020; Randazzo et al., 2020; Roby et al., 2020; Zscheischler et al., 2014; Stoy et al., 2005). However, with existing polar-orbiting satellites we have been largely limited to studying the multi-day to inter-annual variability of GPP rather than its dynamic response to environmental variability across the course of a day. With recent advances in the spectral coverage and spatial resolution of geostationary imagers commonly used for weather mon-

itoring, we argue that we can estimate GPP from space-based observations at sub-daily temporal frequencies (Khan et al., 2021; Xiao et al., 2021). This opens up new opportunities to study the diurnal cycles of GPP and its response to environmental conditions in near real-time (Khan et al., 2021; Xiao et al., 2021). Our ability to develop diurnal estimates of carbon fluxes that can respond to changing environmental conditions will allow us to provide space-based GPP estimates for future model inter-comparison studies and model ensemble estimates at a comparatively higher temporal frequency.

To start estimating GPP at a sub-daily temporal resolution from space-based observations, we can look towards various formulations of GPP's response to light and environmental variability. The development of space-based GPP estimates has largely relied on relationships between the fraction of photosynthetically active radiation (PAR) absorbed by plants (fAPAR) and vegetation indices and Light Use Efficiency (LUE) models that can convert absorbed PAR (APAR) to net primary production (NPP) or GPP (Anderson et al., 2000; Cramer et al., 1999; Field et al., 1995; Joiner et al., 2018; Mahadevan et al., 2008; Running et al., 2004; Xiao et al., 2019; Yuan et al., 2014). Vegetation indices developed from remotely sensed reflectance in visible to near-infrared wavelengths, such as the Normalized Difference Vegetation Index or the Enhanced Vegetation Index, have served as indicators of fAPAR and are often used to estimate APAR in LUE models (Joiner et al., 2018; Mahadevan et al., 2008; Running et al., 2004; Xiao et al., 2019; Yuan et al., 2007). Based on the idea that the near infrared radiation reflected by plants is proportional to the PAR absorbed by plants, the near infrared reflectance of vegetation (NIR_v) has shown strong linear relationships with GPP and can be correlated with fAPAR (Badgley et al., 2017, 2019; Baldocchi et al., 2020; Wu et al., 2020). Furthermore, a radiance based (NIR_v) was also correlated with GPP and APAR across agricultural sites and tropical forest canopies (Merrick et al., 2021; Wu et al., 2020). On the ground, temperature-respiration relationships and light response curves calculated from solar radiation incident on the surface are widely used to partition Net Ecosystem Exchange (NEE) from eddy covariance towers into GPP and ecosystem respiration (R_{eco})(Reichstein et al., 2012; Desai et al., 2008; Lasslop et al., 2010; Stoy et al., 2006). In terms of capturing the impact of environmental variability, this is mainly accomplished by developing environmental stressors from vapor pressure deficit (VPD), air temperature, land surface temperature (LST), and other variables that can capture moisture or temperature stress on GPP (Field et al., 1995; Joiner & Yoshida, 2020; Lasslop et al., 2010; X. Li et al., 2021; Running et al., 2004; Yuan et al., 2007).

The models used to estimate GPP from space-based observations have demonstrated a bias during times of soil moisture stress (Sims et al., 2014; Stocker et al., 2019). However, models that can couple transpiration and carbon uptake have shown success in capturing the response of carbon uptake to soil moisture stress (Anderson et al., 2000). Sub-daily observations from the Advanced Baseline Imager (ABI) on the Geostationary Operational Environmental Satellites - R Series (GOES-R) provide an ideal set of observations to test whether space-based GPP estimates capture the effects of water limitation on GPP. This is because the diurnal course of carbon uptake and water loss shift in a distinct way that can be indicative of soil moisture deficits due to stomatal regulation of water loss (Baldocchi, 1997; Tuzet et al., 2003; Schulze & Hall, 1982). With ongoing projections of increasing drought conditions and heat stress, a key priority for space-based GPP estimates is to capture the impact of water stress. The proper investigation of diurnal water-use efficiency requires that diurnal relationships between GPP and water fluxes are appropriately captured (Nelson et al., 2018) and this should extend to diurnal space-based GPP estimates as well (Xiao et al., 2021).

As we begin to leverage the wealth of sub-daily temporal information available from the ABI that has similar spectral sensitivity to MODIS and Landsat (Schmit & Gunshor, 2020), we need to assess how the diurnal patterns of ecosystem carbon uptake estimated from remote sensing compare with our current understanding of diurnal patterns

in ecosystem carbon uptake. Stomatal regulation through adjustments in stomatal conductance is the dominant mechanism by which carbon uptake and water loss are coupled in plants(Cowan & Farquhar, 1977). There are various physiological and environmental signals that exert a control on stomatal conductance such as CO_2 concentrations inside the leaf, sugar accumulation, leaf and guard cell water potential, VPD, and PAR (Grossiord et al., 2020; Jalakas et al., 2021; Lawson, 2009; Matthews et al., 2017; Meinzer et al., 2017; Novick et al., 2016). PAR and VPD have been recognized as the dominant environmental drivers of NEE and GPP at diurnal scales if soil moisture, temperature, and vegetation phenology do not limit photosynthesis (Stoy et al., 2005). However, during times of soil moisture stress, the diurnal course of stomatal conductance, carbon uptake, and water loss do not always follow the symmetric course of solar radiation due to additional controls on stomatal conductance (Schulze & Hall, 1982). Diurnal asymmetry in ecosystem fluxes of carbon and water have been identified across various climates and plant functional types resulting in differences in these fluxes between the morning and afternoon and a shift in peak GPP to morning hours (Anderson et al., 2008; Baldocchi, 1997; Bucci et al., 2019; Lasslop et al., 2010; Lin et al., 2019; Konings, Yu, et al., 2017; Matheny et al., 2014; Nelson et al., 2018; K. B. Wilson et al., 2003). The diurnal shift of peak GPP and evapotranspiration (ET) has been shown to vary closely with moisture availability because the increased VPD during the afternoons in the face of low soil moisture can result in stomatal closure during the afternoon (Matthews et al., 2017; Nelson et al., 2018; Schulze & Hall, 1982). If geostationary satellites can capture these dynamics, we can strengthen our basis for estimating sub-daily GPP from space.

Here, we provide diurnal estimates of GPP at a 30-minute temporal resolution using five-minute mulitspectral data from the Advanced Baseline Imager (ABI) on board the Geostationary Operational Environmental Satellites - R Series (GOES-R) and other sub-daily products from the GOES-R ABI along with estimates of GPP from the Tonzi Ranch (US-Ton) Ameriflux eddy covariance tower in California, USA. During the dry summers, the Tonzi Ranch experiences low precipitation and low soil moisture characteristic of its Mediterranean climate. This provides an ideal case study to test the ability of widely-used models and ABI-based estimates of APAR to ask: How well can diurnal estimates of GPP based on radiation inputs from ABI capture diurnal and seasonal patterns in GPP at a site experiencing seasonal soil moisture deficits? We analyze the diurnal peaks of GPP and latent heat flux (LE) to test whether ABI-based GPP estimates can capture the shifting diurnal patterns of CO_2 uptake and water loss that can be indicative of soil moisture stress at this site. We also focus our discussion on opportunities to extend GPP estimation using ABI to other ecosystems including key uncertainties that need to be addressed to advance our ability to monitor GPP in near-real time.

2 Materials and Methods

2.1 Study site

Our study site is an oak savanna Ameriflux eddy covariance site located at the Tonzi Ranch at the foothills of the Sierra Nevada mountain range near Ione, CA (38.4309 N, -120.9660 W, 177 m asl). The annual mean air temperature from 1926 - 2016 near the site was reported as $16.6°C$ and the average annual precipitation was reported as 546 mm (Ma et al., 2020). The rainy season can last from October to April and is characterized by lower levels of incoming solar radiation, net radiation, VPD, and lower diurnal variation in temperatures (i.e. the difference between daily maximum and minimum temperatures) (Baldocchi et al., 2004; Xu & Baldocchi, 2003). The site experiences clear days, the highest levels of incoming solar radiation, and very little to no precipitation during the summer months (Baldocchi et al., 2004; Xu & Baldocchi, 2003). The site also experiences the highest VPD during the year along with rapidly declining soil moisture during the summer (Baldocchi et al., 2004, 2021; Xu & Baldocchi, 2003). Diurnal vari-

ation in temperature also increases during the summer months (Xu & Baldocchi, 2003).
For our study, we characterized the seasons experienced at our site according to Ma et
al. (2016) as: winter (Jan. - Mar.), spring (Apr. - Jun.), summer (Jul. - Sep.), and fall
(Oct. - Dec.).

Blue oak trees (*Quercus douglassi*) make up the deciduous overstory of the oak sa-
vanna while the understory consists of C_3 annual grassses and herbs (Baldocchi et al.,
2004; Ma et al., 2020). The tree canopy is dormant during the rainy winter and leafs out
during the spring and reaches full photosynthetic capacity (Xu & Baldocchi, 2003). The
rainy season provides soil moisture for the trees which is drawn down gradually through
transpiration into the summer months (Baldocchi et al., 2004; Ma et al., 2016). The tree
canopy is able to maintain photosynthesis and transpiration during the dry season through
the ability to regulate water loss and access of some roots to ground water (Baldocchi
et al., 2004). The trees lose their leaves in late autumn and the understory grasses ger-
minate after the first rainfall of autumn (Baldocchi et al., 2004; Ma et al., 2016). The
understory grows throughout the winter and spring, but dies before the dry summer months
(Ma et al., 2020; Baldocchi et al., 2004). Both GPP and evapotranspiration peak dur-
ing the spring after the trees become photosynthetically active (Baldocchi et al., 2021;
Ma et al., 2016, 2020). The soil is an Auburn very rocky silty loam with 37.5 - 48 % sand,
42 - 45 % silt, and 10 - 17.5 % clay depending on under canopy or open space areas (Baldocchi
et al., 2004).

2.2 Data

2.2.1 ABI

We used the GOES-R ABI Level 1b top-of-atmosphere (TOA) radiances (ABI-L1b-
RadC) from GOES-16 and GOES-17. ABI-L1b-RadC is delivered at a five-minute tem-
poral resolution over the conterminous United States (CONUS). The spatial resolution
of the near-infrared (NIR) band (central wavelength: $0.86\,\mu m$) is 1 km at nadir and the
spatial resolution of the red band (central wavelength: $0.64\,\mu m$) is 0.5 km at nadir (Schmit
& Gunshor, 2020). The red band TOA radiance was aggregated to the 1 km at nadir
scale using the median TOA radiance. ABI-L1b-RadC is available on Amazon Web Ser-
vices and was accessed with S3Fs, a python module for accessing Amazon S3 buckets
with ABI data. The TOA radiances (L_{toa}) were converted to TOA reflectance factors
(ρf_{toa}) as described in the GOES-R Product Definition and User's Guide (PUG) (NASA,
2019):

$$\rho f_{toa} = \kappa L_{toa} \tag{1}$$

$$\kappa = \frac{\pi d^2}{E_{sun}} \tag{2}$$

where d is the Earth-Sun distance (Astronomical Units) and E_{sun} is the solar ir-
radiance for a given band ($Wm^{-2}\mu m^{-1}$) (NASA, 2019). κ, d, and E_{sun} are provided in
the product metadata for each band (NASA, 2019). The five-minute ABI Level 2 Clear
Sky Mask for CONUS (ABI-L2-ACMC) was used to identify clear observations. ABI-
L2-ACMC and the hourly Downward Shortwave Radiation (DSR) (ABI-L2-DSRC) (NASA,
2018) were downloaded through the National Oceanic and Atmospheric Administration's
Comprehensive Large Array-Data Stewardship System (CLASS). At the coordinates of
the Tonzi Ranch, we extracted the TOA reflectance factors for the NIR band and the
red band calculated from ABI-L1b-RadC along with DSR values from ABI-L2-DSRC
and clear/cloudy flags from ABI-L2-ACMC. Quality flags provided in the metadata of
ABI-L1b-RadC and the clear sky flag from ABI-L2-ACMC were used to identify clear

Table 1: Number of clear sky and good quality observations available from 5-minute ABI-L1b-RadC and hourly ABI-L2-DSRC by season and the ABI on GOES-16 (16) and GOES-17 (17).

Season	ABI	ABI-L1b-RadC	ABI-L2-DSRC
Winter	16	18494	1233
Winter	17	15366	1216
Spring	16	24761	1853
Spring	17	25877	1867
Summer	16	35324	1828
Summer	17	31798	1825
Fall	16	32467	1108
Fall	17	24644	1102

and good quality observations from ABI-L1b-RadC to estimate surface reflectance. Table 1 shows the number of good quality clear observations from ABI-L1b-RadC and ABI-L2-DSRC for each season.

The surface bidirectional reflectance was estimated from TOA bidirectional reflectance factors from ABI using the radiative transfer equations of Qin et al. (2001) as previously used by He et al. (2019) to estimate surface reflectance from ABI TOA data. Similar to previous efforts with ABI and MODIS data (He et al., 2012, 2019), we used The Second Simulation of a Satellite Signal in the Solar Spectrum (6S) radiative transfer model with the python-based Py6S (R. Wilson, 2013) to estimate the following atmospheric parameters with the assumption of a Lambertian ground reflectance: path reflectance, spherical albedo, atmospheric transmittance, direct fraction of incoming radiation, diffuse fraction of incoming radiation, and spectral irradiance. The surface anisotropy of reflected radiation was characterized by the Ross-Thick volumetric kernel, K_{vol}, and the Li-Sparse geometric kernel, K_{geo} (Wanner et al., 1995). The Bidirectional Reflectance Distribution Function (BRDF) was estimated as:

$$R(\theta_s, \theta_v, \phi_r) = f_{iso} + f_{vol}\, K_{vol}(\theta_s, \theta_v, \phi_r) + f_{geo}\, K_{geo}(\theta_s, \theta_v, \phi_r) \qquad (3)$$

where θ_s is the solar zenith angle (SZA), θ_v is the the view zenith angle (VZA), and ϕ_r is the relative azimuth angle. We estimated f_{iso}, f_{vol}, and f_{geo} through minimizing a least squares cost function between the TOA reflectance factor observed by the ABI on GOES-16 and GOES-17 and the TOA reflectance factor estimated by the radiative transfer model of Qin et al. (2001). The BRDF coefficients were estimated using observations collected at an SZA less than 70 degrees for each day when there were at least 10 observations available during the day for the red and NIR ABI bands. For each day, the VZA from GOES-16 and GOES-17 along with diurnally varying SZA at five-minute intervals was used to fit the BRDF model. We used discrete values of aerosol optical depth at 550 nm (AOD) as explained in He et al. (2019) with different aerosol types (biomass burning, continental, maritime, urban, and stratospheric) to estimate atmospheric parameters from 6S. The AOD and and aerosol type combination that resulted in the smallest least squares cost function between observed and estimated TOA reflectance was used as the values for AOD and aerosol type for the day. To approximate surface reflectance at nadir viewing, we calculated the geometric and volumetric kernels at each SZA value during the day with a fixed VZA of 0 degrees. Then, we used the BRDF kernel coefficients (f_{iso}, f_{vol}, f_{geo}) to estimate the surface reflectance at nadir throughout the day.

259   *2.2.2 Ameriflux eddy covariance tower*

260   Instrumentation to measure micrometeorological variables and fluxes were installed
261 on a 23 m tower $\sim$ 10 m above the tree canopy and a separate set of understory flux
262 measurements were collected 2 m above the ground (Baldocchi et al., 2021; Ma et al.,
263 2001). Wind velocity was measured with a three-dimensional ultrasonic anemometer (Wind-
264 Master, Gill Instruments) and CO_2 and water vapor fluxes were measured at 10 - 20 times
265 per second using an open-path infrared absorption gas analyzer (LI-7500A, LICOR) (Baldocchi
266 et al., 2004, 2021). NEE was calculated using the eddy covariance technique and the par-
267 titioned GPP and R_{eco} were provided to Ameriflux (Baldocchi et al., 2021; Ma et al.,
268 2001). Upward and downward facing quantum sensors (PAR-LITE, Kipp & Zonen) and
269 a net radiometer consisting of upward and downward facing pyranometers and pyrge-
270 ometers (CNR1, Kipp & Zonen) (Baldocchi et al., 2021) measure broadband radiation
271 flux densities in photosynthetically active (400 - 700 nm), shortwave (305 - 2800 nm),
272 and longwave (5000 - 50,000 nm) regions. Incident and reflected narrow band radiation
273 in the red (central wavelength: 650 nm) and NIR (central wavelength: 810 nm) regions
274 was measured with spectral reflectance sensors (SRS-Ni NDVI, Decagon-METER) with
275 a hemispherical 180° field of view (Baldocchi et al., 2020). Air temperature and relative
276 humidity were measured with a platinum resistance temperature detector and humicap
277 (HMP45AC, Vaisala). A set of segmented time domain reflectometry probes (Moisture
278 Point PRB-K, Environmental Sensors Inc.) and Theta probes (ML2x, Delta-D Devices)
279 measure volumetric soil moisture content at depths of 5 - 60 cm (Baldocchi et al., 2021;
280 X. Chen et al., 2008).

281   The cumulative daytime footprint around the overstory tower from where 80 % of
282 the fluxes originate covers oak trees, the understory layer, and open spaces of the savanna
283 (Ma et al., 2020). The footprint fetch is asymmetric around the tower and varied between
284 318 - 384 m during the daytime and 648 - 866 m during nighttime for 2014 - 2017 (Chu
285 et al., 2021). The area of the footprint varied between 234,771 m^2 - 230,237 m^2 during
286 the day and 419,838 m^2 - 656,611 m^2 at night (Chu et al., 2021). The dominant land
287 cover type is classified as grassland/herbaceous in the National Landcover Database and
288 makes up a little over 50 % of the area that is 1000 - 3000 m around the tower (Chu et
289 al., 2021). The site's footprint's representativeness of its surroundings is classified as medium
290 at scales of 1000 - 3000 m around the tower during the day (Chu et al., 2021). Previ-
291 ous analysis of energy balance closure at the site with a linear regression between net
292 radiation and the sum of sensible heat flux, latent heat flux, soil heat flux, and canopy
293 heat storage has resulted in an intercept of -10.6 $W\,m^{-2}$ and a slope of 1.04 ($r^2 = 0.94$)
294 (Baldocchi et al., 2004). Data collected under heavy rainfall (> 10 mm) were removed
295 (Baldocchi et al., 2021).

296   The hourly ABI DSR data were linearly interpolated to the half-hour temporal res-
297 olution of the Ameriflux data. Vegetation indices were calculated from the clear sky, 5-
298 minute, nadir-adjusted surface reflectance estimates. The midday medians of the veg-
299 etation indices for each day were calculated between hour 10 and 14. Finally, we used
300 all available daytime data with a solar zenith angle of less than 70 degrees from 2019 -
301 2020 from ABI and Ameriflux for GPP estimation.

302   **2.3 Estimating GPP**

303   GPP was estimated using a light-use efficiency model (LUE-NDVI), a linear rela-
304 tionship between the product of NIR_v and PAR (NIR_vP) and GPP (LIN-NIR_vP), and
305 a light response curve between NIR_vP and GPP. The normalized difference vegetation
306 index (NDVI) calculated from ABI surface reflectance was used in the LUE-NDVI model
307 (Running et al., 2004). NIR_v calculated from ABI surface reflectance was used in the
308 LIN-NIR_vP model and the light response curve between NIR_vP and GPP (Baldocchi et
309 al., 2020; Dechant et al., 2020). The midday median value of NDVI and NIR_v were used.

310 The LUE-NDVI model was specified as (Running et al., 2004):

$$GPP = \epsilon_{max} \, T_{scale} \, W_{scale} \, APAR \tag{4}$$

312 where ϵ_{max} is the maximum canopy LUE ($\mu mol \, CO_2 \, J^{-1}$) under ideal environmental con-
313 ditions and APAR is absorbed photosynthetically active radiation (PAR) ($W \, m^{-2}$) and
314 is calculated as:

$$APAR = fAPAR \times PAR \tag{5}$$

316 where fAPAR is the fraction of absorbed PAR and is approximated by the daily mid-
317 day median NDVI. NDVI was calculated as:

$$NDVI = \frac{\rho_{NIR} - \rho_{Red}}{\rho_{NIR} + \rho_{Red}} \tag{6}$$

319 where ρ_{NIR} is the reflectance in the ABI NIR band and ρ_{Red} is the reflectance in the
320 ABI red band. PAR was estimated as (Meek et al., 1984; Weiss & Norman, 1985):

$$PAR = 0.45 \, DSR \tag{7}$$

322 where DSR is the linearly interpolated ABI Downward Shortwave Radiation from ABI-
323 L2-DSRC. We calculated T_{scale} and W_{scale} according to the MODIS LUE model (Running
324 & Zhao, 2015). T_{scale} was calculated as (Huang et al., 2021; Running & Zhao, 2015):

$$T_{scale} = \begin{cases} 0, & \text{if } T_{air} \leq T_{min} \\ \frac{T_{air}-T_{min}}{T_{max}-T_{min}}, & \text{if } T_{min} < T_{air} < T_{max} \\ 1, & \text{if } T_{air} \geq T_{max} \end{cases} \tag{8}$$

326 where $T_{air}(^\circ C)$ is the air temperature measured at the EC tower. $T_{min}(^\circ C)$ is the
327 temperature at which LUE is minimum (LUE $= 0 \, \mu mol \, CO_2 \, J^{-1}$) at any VPD value and
328 $T_{max}(^\circ C)$ is the temperature, under ideal VPD, at which LUE is maximum (LUE $= \epsilon_{max}$)
329 (Running & Zhao, 2015). W_{scale} was calculated as (Huang et al., 2021; Running & Zhao,
330 2015):

$$W_{scale} = \begin{cases} 1, & \text{if } VPD \leq VPD_{min} \\ \frac{VPD_{max}-VPD}{VPD_{max}-VPD_{min}}, & \text{if } VPD_{min} < VPD < VPD_{max} \\ 0, & \text{if } VPD \geq VPD_{max} \end{cases} \tag{9}$$

332 where $VPD(hPa)$ is the vapor pressure deficit from the EC tower. $VPD_{min}(hPa)$ is the
333 VPD at which LUE is maximum (LUE $= \epsilon_{max}$) and $VPD_{max}(hPa)$ is the VPD at which
334 LUE is minumum (LUE $= 0 \, \mu mol \, CO_2 \, J^{-1}$) (Running & Zhao, 2015). The linear rela-
335 tionship between NIR_vP and GPP was approximated as:

$$GPP = \epsilon_{ref} \, NIR_vP \tag{10}$$

337 where ϵ_{ref} is the slope between GPP and NIR_vP. NIR_vP was calculated as (Dechant
338 et al., 2020):

$$NIR_vP = NIR_v \times PAR \tag{11}$$

340 NIR_v was calculated as (Badgley et al., 2017):

$$NIR_v = \rho_{NIR} \, NDVI \tag{12}$$

342 We estimated the GPP term using a light response curve between EC tower partitioned
343 GPP and ABI NIR_vP:

$$GPP = \frac{\alpha \, NIR_vP \, \beta}{\beta + \alpha \, NIR_vP} \tag{13}$$

345 where α is the canopy LUE before light saturation is reached ($\mu mol \, CO_2 \, J^{-1}$) or the ini-
346 tial slope of the relationship between GPP and NIR_vP and β is the maximum CO_2 up-
347 take rate at the point of light saturation ($\mu mol \, CO_2 \, m^{-2} \, s^{-1}$) (Reichstein et al., 2012;

Lasslop et al., 2010). Light response curves can be used to partition NEE into GPP and R_{eco} using incoming solar radiation at the surface (Lasslop et al., 2010). In this case, α is directly approximated as the initial LUE of the incident light response. When replacing incoming solar radiation with NIR_vP, a more specific description of α would be the initial amount of CO_2 taken up with increases in NIR_vP (Figure 1). NIR_vP's proportionality with APAR is the basis by which an NIR_vP-based α could approximate an APAR based α. The impact of increasing VPD and the resulting stress on the maximum CO_2 uptake rate at light saturation, β, was estimated according to Lasslop et al. (2010) (Figure 2):

$$\beta = \begin{cases} \beta_0 \, exp(-k\,(VPD - VPD_0)), & \text{if } VPD > VPD_0 \\ \beta_0, & \text{otherwise} \end{cases} \tag{14}$$

where k is the sensitivity of the maximum CO_2 uptake rate at light saturation, β, to VPD. β_0 is the maximum CO_2 uptake rate at light saturation during conditions of ideal VPD ($VPD < VPD_0$). VPD_0 was set as 10 hPa (Lasslop et al., 2010). Atmospheric VPD from the EC tower was used here.

We estimated ϵ_{max}, T_{min}, T_{max}, VPD_{min}, VPD_{max}, ϵ_{ref}, α, β_0, and k through minimization of a cost function implemented in the Python-based open-source software, SciPy (Virtanen et al., 2020) as:

$$minimize\,0.5 \times \sum_{i=1}^{n} \rho_i \tag{15}$$

To reduce the influence of outliers, the Huber loss function was used to calculate the vector ρ which is also implemented in the Python-based open-source software, SciPy (Virtanen et al., 2020) as:

$$\rho = \begin{cases} z & \text{if } z \leq 1 \\ 2\sqrt{z} - 1 & \text{otherwise} \end{cases} \tag{16}$$

where z is a vector of the squared errors between estimated GPP and EC tower GPP for a daytime half hour i in $1, ..., n$ during the month for the two years of data. We estimated parameters for each month separately using 2 years of diurnal observations. Seventy percent of the data for a given month was used for estimating the parameters and 30 % was used to test GPP estimates from the models against EC tower GPP. The data was split into test and training data using the python module Scikit-learn (Pedregosa et al., 2011). To test the impact of NEE partitioning, we also estimated all parameters using GPP partitioned from two different NEE partitioning approaches in addition to the Ameriflux provided GPP (Appendix B).

2.4 Model evaluation

We used a robust regression implemented in Python's statsmodels module to fit a linear model between the ABI GPP estimates and the EC tower GPP estimates using our test and training data (Seabold & Perktold, 2010). For each model used to estimate GPP from ABI inputs, a linear model was fit by gathering the training and test data used for each month into one training and test set for the 2 year study period. Furthermore, the training and test data used for each month were also pooled into seasonal training and test data for each model. We used these seasonal pools of training and test data to calculate the mean absolute error , the normalized mean absolute error, and the mean error between ABI GPP estimates and EC tower GPP estimates for each season. These error summaries were calculated as:

$$Mean\,Error = \frac{\sum_{i=1}^{n} \widehat{GPP_i} - GPP_i}{n} \tag{17}$$

$$Mean\,Absolute\,Error = \frac{\sum_{i=1}^{n} |\widehat{GPP_i} - GPP_i|}{n} \tag{18}$$
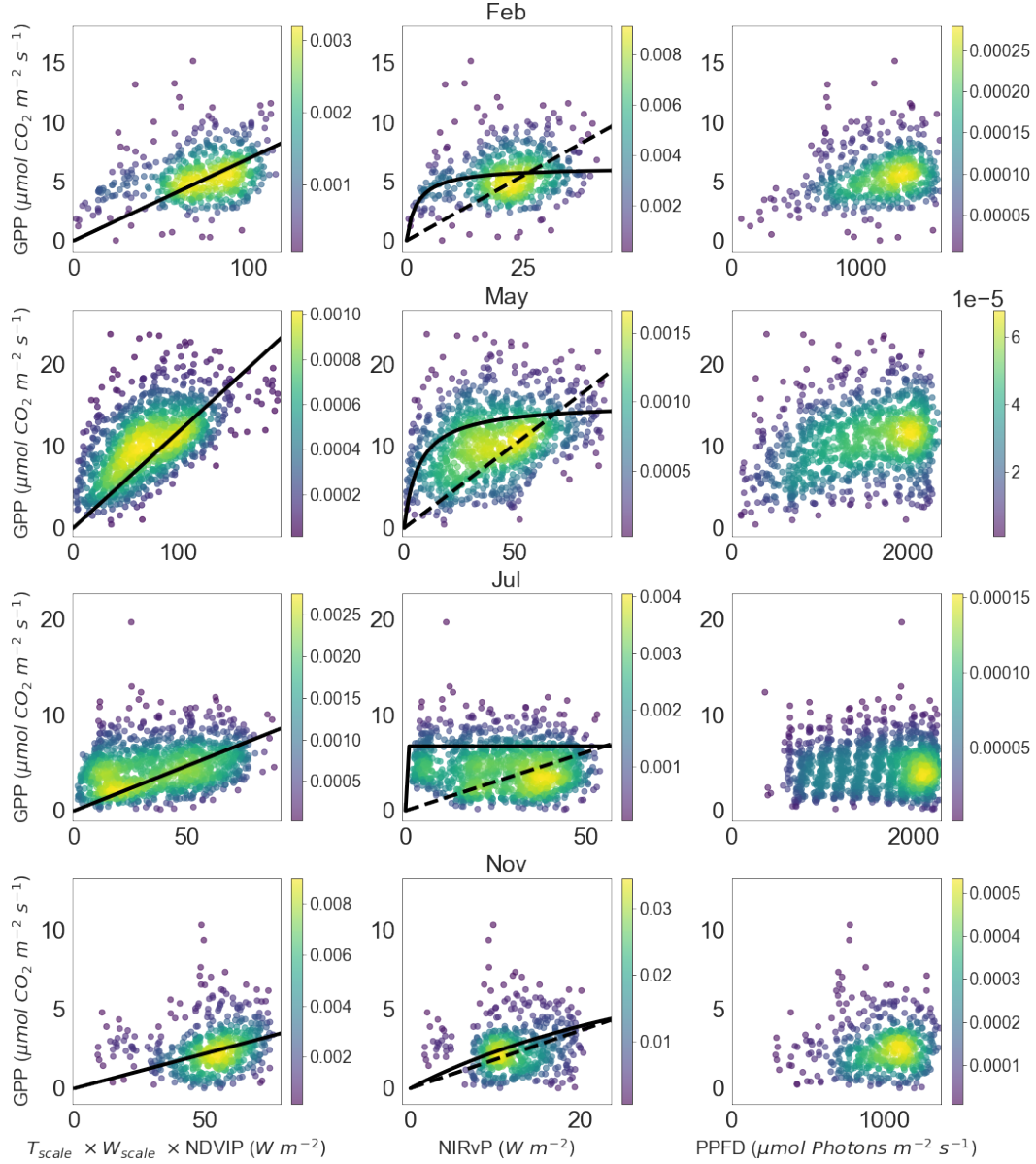
Figure 1: Eddy covariance tower GPP vs. ABI normalized difference vegetation index (NDVI) × photosynthetically active radiation (NDVIP) × the environmental stresses developed for the LUE-NDVI model (first column). The black line displays the GPP estimates from the LUE-NDVI model. The response of eddy covariance tower GPP to the ABI near-infrared reflectance of vegetation × PAR (NIR_vP) (second column). The dashed black line displays the GPP estimates using the LIN-NIR_vP model. The solid black line displays the GPP estimates from the LRC-VPD model with $\beta = \beta_0$. The response of GPP to the photosynthetic photon flux density measured at the eddy covariance tower (third column).
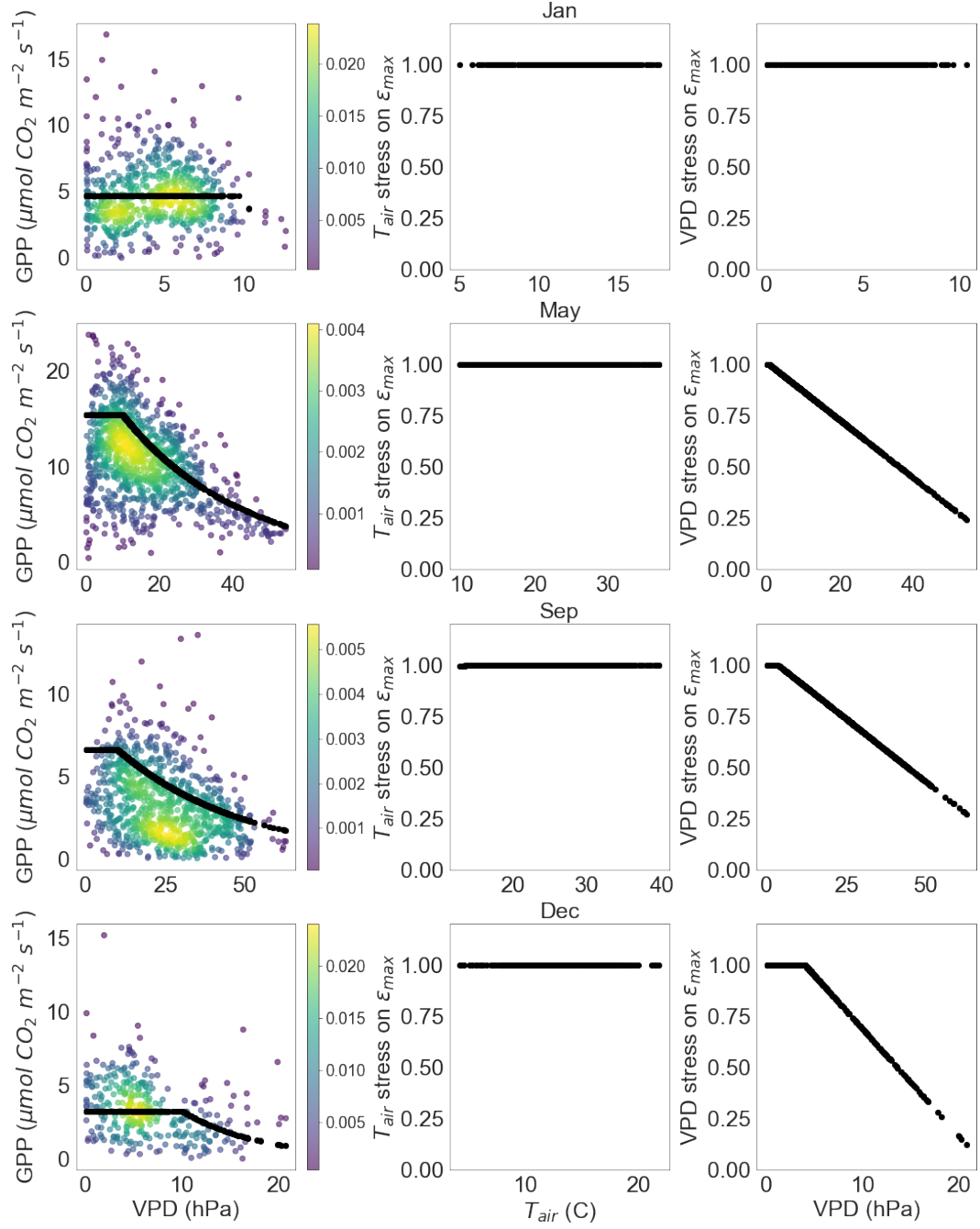
Figure 2: The response of GPP to vapor pressure deficit (VPD) (1st column). The black lines shows the values of β estimated using equation 14. The air temperature (2nd column) and VPD stress (3rd column) on ϵ_{max} from the LUE-NDVI model. A value of 1 means there is no stress and 0 means the stress on ϵ_{max} is maximum.

393

394
$$Normalized\,Mean\,Absolute\,Error = \frac{Mean\,Absolute\,Error}{\overline{GPP}} \qquad (19)$$

395 where $\widehat{GPP}_i$ is the ABI-based estimate of GPP and GPP_i is the EC tower estimate of
396 GPP for a daytime half hour i in $1, ..., n$ in a given season. $\overline{GPP}$ is the seasonal mean
397 of daytime EC tower estimates of GPP.

398 A reflectance based NIR_v could be proportional to the fraction of absorbed PAR
399 and NIR_vP could be proportional to a radiance-based NIR_v which has shown propor-
400 tionality to APAR (Wu et al., 2020). Therefore, the difference between NIR_vP and in-
401 cident PAR could be indicative of the differences between incident PAR and APAR. We
402 tested if using NIR_vP in the light response curve rather than incident PAR contributed
403 to the errors between $\widehat{GPP}$ and GPP. We compared the errors from each model to the
404 difference between a PPFD based NIR_vP and incident PPFD measured at the EC tower
405 as: $NIR_vP_{PPFD}-PPFD$. To match the units of tower PPFD, PAR (Wm^{-2}) calcu-
406 lated from ABI DSR was converted to PAR in PPFD units $(\mu mol\,Photons\,m^{-2}\,s^{-1})$ as
407 (Thimijan & Heins, 1983):

$$PPFD_{ABI} = 4.57\,\mu mol\,Photons\,J^{-1} \times PAR \qquad (20)$$

408 NIR_vP_{PPFD} was calculated as:

$$NIR_vP_{PPFD} = NIR_v \times PPFD_{ABI} \qquad (21)$$

409 **2.5 Diurnal centroids**

410 The diurnal centroid method (Nelson et al., 2018; K. B. Wilson et al., 2003) was
411 used to compare diurnal patterns in water loss and carbon uptake between ABI estimates
412 of GPP and EC tower estimates. A diurnal centroid for a given flux was calculated as
413 (Nelson et al., 2018; K. B. Wilson et al., 2003):

414
$$C_{flux} = \frac{\sum_{t=9}^{15} flux_t\,t}{\sum_{t=9}^{15} flux_t} \qquad (22)$$

415 where t is the time in decimal hours from the daylight hours of 9 - 15. We only used days
416 when continuous cloud-free observations were available between these hours to calculate
417 the diurnal centroid. C_{flux} has been used as an indicator of diurnal asymmetry in ecosys-
418 tem fluxes of water and CO_2 (Nelson et al., 2018; K. B. Wilson et al., 2003). For exam-
419 ple a C_{flux} less than 12 would indicate a shift of the flux towards the morning hours and
420 a C_{flux} of greater than 12 would indicate a shift of the flux towards the afternoon (K. B. Wil-
421 son et al., 2003). Furthermore, the difference between the diurnal centroids of different
422 fluxes was used to study the (mis)alignment of peak fluxes throughout year (K. B. Wil-
423 son et al., 2003). To compare the departure of peak GPP from diurnal peak solar radi-
424 ation, we took the difference between the diurnal centroids of all GPP estimates from
425 the diurnal centroid of incoming shortwave (SW) radiation measured at the EC tower
426 (Nelson et al., 2018).

427
$$C_{GPP*} = C_{GPP} - C_{SW_{in}} \qquad (23)$$

428 The shift of both peak GPP and ET to morning hours could imply declining soil
429 moisture (K. B. Wilson et al., 2003). To test whether the (mis)alignment of diurnal peak
430 GPP and LE using ABI-based GPP estimates agreed with EC tower (mis)alignment of
431 the diurnal peaks of these two fluxes with varying soil moisture throughout the year, we
432 also calculated the daily diurnal centroid of EC tower LE. For each GPP estimate, the
433 difference between the centroids of GPP and EC tower LE was calculated as:

434
$$C_{GPP-LE} = C_{GPP} - C_{LE} \qquad (24)$$

3 Results

3.1 Model evaluation

Estimates of GPP using LRC-VPD achieved the lowest mean error, mean absolute error, and normalized mean absolute error for the training data during all seasons (Table 2). The lowest training normalized mean absolute error (0.26) was achieved during the spring season and the highest (0.45) was during the fall. Among the test data, LRC-VPD GPP estimates also achieved the lowest mean error, mean absolute error, and normalized mean absolute error during all seasons (Table 2). Similar to the training data, the lowest test normalized mean absolute error (0.26) was during the spring and the highest test normalized mean absolute error was during the fall (0.43). All models used resulted in an underestimate of GPP compared to EC tower GPP during all seasons among the training and test data with the exception of winter test data (Table 2).

Diurnal GPP estimates from LRC-VPD and LUE-NDVI follow the diurnal course of EC tower estimates of GPP more closely compared to the LIN-NIR$_v$P GPP during the spring and summer (Figure 3). LRC-VPD GPP estimates appear to follow the shift of peak GPP towards the morning hours during the summer. None of the models are able to capture some of the higher diurnal peaks in GPP during all four seasons (Figure 3). The LRC-VPD GPP estimates also show better agreement with the course of seasonal half-hourly means of GPP from EC tower estimates during all seasons during the study period (Figure 4).

The robust regression between GPP estimated with ABI inputs and EC tower GPP revealed a similar divergence from a 1:1 relationship among all three models and training and test data (Figure 5). At low EC tower GPP values, GPP estimates from all three models were slightly higher and at high EC tower GPP values, GPP estimates from all three models were lower (Figure 5). A robust regression between the daily median GPP estimates resulted in relationships that were closer to the 1:1 line for all three models (Figure 5). The errors between EC tower GPP and estimates of GPP from the LRC-VPD show a tendency of the LRC-VPD to underestimate EC tower GPP during times of much higher incident PPFD relative to NIR$_v$P$_{PPFD}$ ($NIR_v P_{PPFD} - PPFD < -1500\,\mu mol\,Photons\,m^{-2}\,s^{-1}$)(Figure 6). These pattern are consistent when using both ABI NIR$_v$P$_{PPFD}$ and EC tower NIR$_v$P$_{PPFD}$ (Figure 6).

3.2 Diurnal centroids

Data on GPP, LE, and soil water content in the top 15 cm from the EC tower reveal that the soil water content in this layer declines rapidly from April to June and the lowest soil water content occurs during July - November (Figure 7). C$_{GPP}$ is shifted increasingly earlier in the day matching the rapid decline in soil water content through May, June, and July (Figure 7). During times of low soil water content, C$_{LE}$ also shifted to earlier in the day; it occurred after C$_{SW_{in}}$ during the spring and early summer and before C$_{SW_{in}}$ during the months with the lowest soil water content (Figure 7). Since VPD peaks during the afternoon throughout the year, C$_{LE}$ and C$_{GPP}$ became increasingly aligned as soil water content decreased (Figure 7). Below we discuss the results for how these diurnal patterns in the (mis)alignment of C$_{LE}$ and C$_{GPP}$ compare with our estimates of GPP from the LRC-VPD, LIN-NIR$_v$P, and LUE-NDVI models.

The diurnal centroids of EC tower GPP and GPP estimates from the LRC-VPD and LUE-NDVI models reveal shifting peaks in GPP towards earlier in the day as the ecosystem experiences decreasing soil moisture with the progression into the summer months (Figure 7). The EC tower GPP estimates resulted in the largest
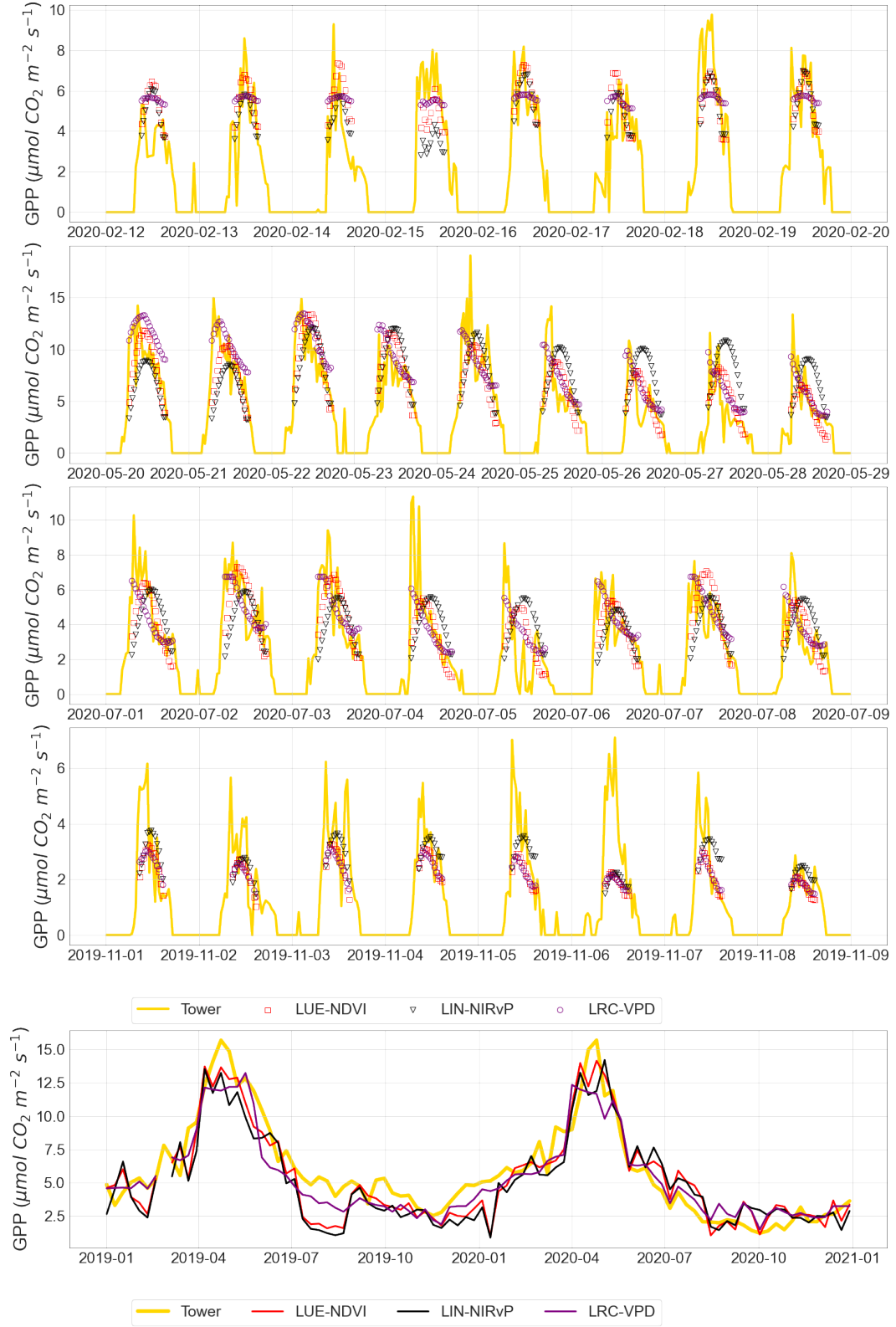
Figure 3: Subsets of seasonal time series of estimates of GPP from all models compared to estimates of GPP from the eddy covariance tower. The bottom plot shows 8-day means for all GPP estimates for the study period.
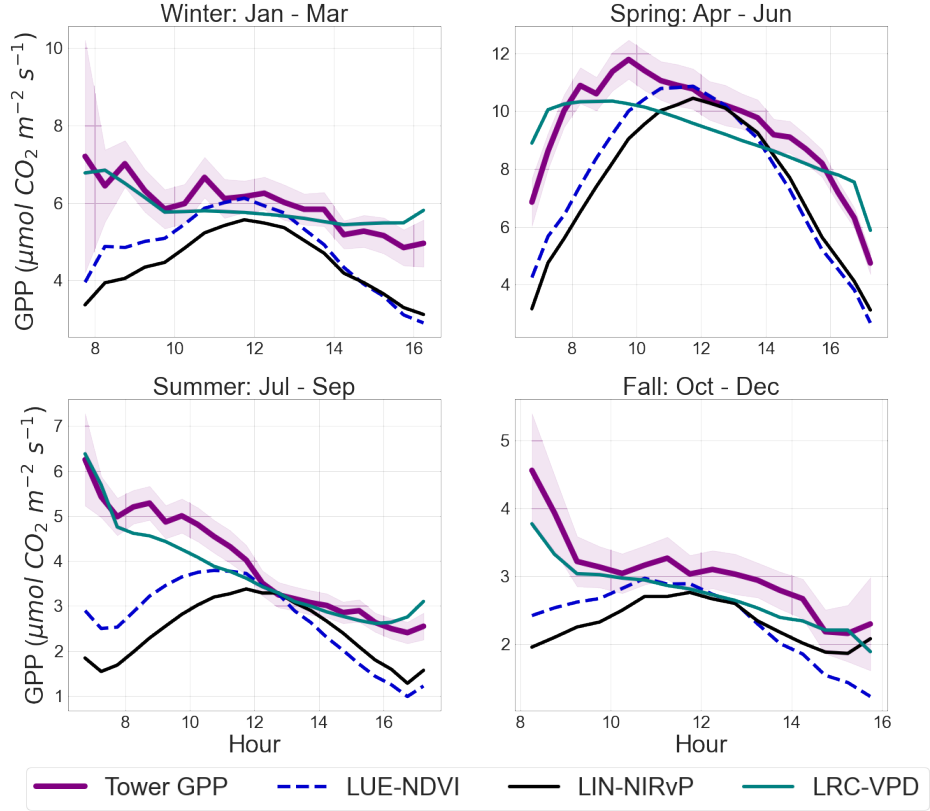
Figure 4: Seasonal diurnal means of estimates of GPP from all models and diurnal means of estimates of GPP from the eddy covariance tower. The purple shaded region shows ± 2 standard error of the mean eddy covariance tower GPP. The data spans from Jan 2019 - Dec 2020. The mean diurnal cycle estimated from LRC-VPD GPP estimates is best able to respond to the increasing diurnal asymmetry in GPP in the summer months. LUE-NDVI GPP estimates result in mean diurnal cycles that are able to shift slightly towards morning peaks during the summer. LIN-NIR$_{v}$P GPP estimates result in symmetric mean diurnal cycles throughout the year.

Table 2: Comparison of mean error (ME), mean absolute error (MAE), and normalized MAE (NMAE) between ABI based GPP estimates and eddy covriance tower GPP estimates. The units for ME and MAE are $\mu mol\, CO_2\, m^{-2}\, s^{-1}$.

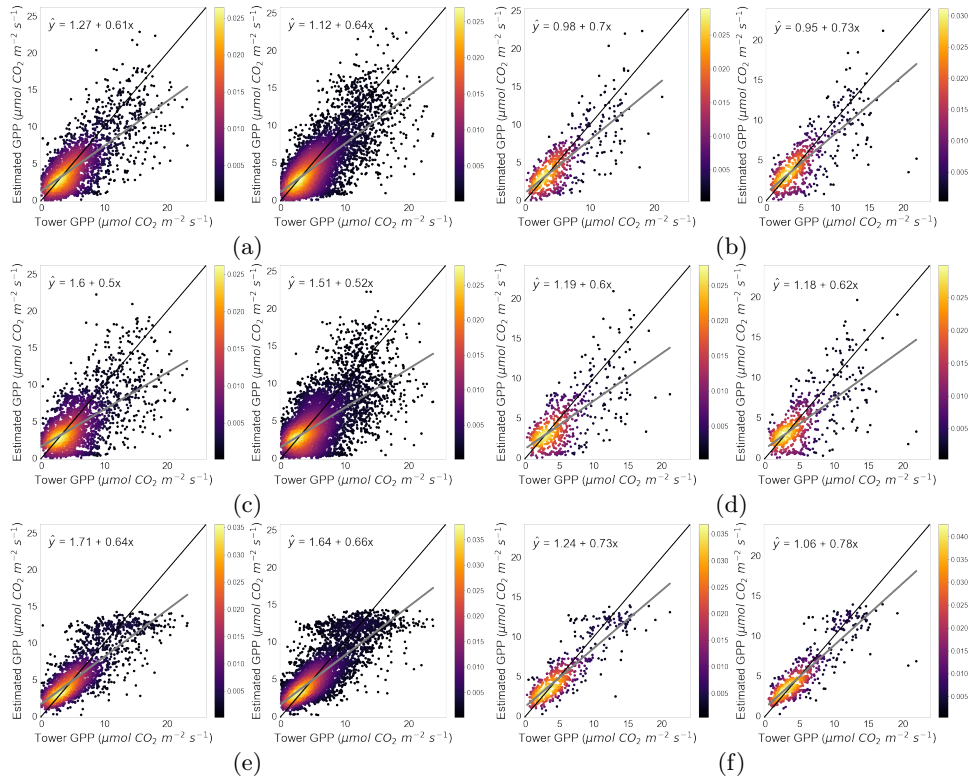| Season	Model	Training data			Test data		
		ME	**MAE**	**NMAE**	**ME**	**MAE**	**NMAE**
Winter	LIN-NIR$_v$P	−0.764	2.340	0.388	−0.629	2.313	0.402
Winter	LUE-NDVI	−0.504	2.042	0.339	−0.380	2.072	0.360
Winter	LRC-VPD	**−0.189**	**1.772**	**0.294**	**0.041**	**1.816**	**0.316**
Spring	LIN-NIR$_v$P	−1.152	3.454	0.372	−1.491	3.549	0.371
Spring	LUE-NDVI	−0.967	2.953	0.318	−1.230	3.066	0.320
Spring	LRC-VPD	**−0.210**	**2.384**	**0.257**	**−0.419**	**2.506**	**0.262**
Summer	LIN-NIR$_v$P	−1.252	2.287	0.599	−1.269	2.382	0.610
Summer	LUE-NDVI	−1.013	2.010	0.526	−0.991	2.068	0.529
Summer	LRC-VPD	**−0.162**	**1.444**	**0.378**	**−0.187**	**1.448**	**0.371**
Fall	LIN-NIR$_v$P	−0.474	1.629	0.548	−0.391	1.449	0.504
Fall	LUE-NDVI	−0.379	1.486	0.500	−0.345	1.375	0.478
Fall	LRC-VPD	**−0.194**	**1.348**	**0.454**	**−0.186**	**1.249**	**0.434**

Figure 5: For each pair of plots a - f, scatter plots of test data (left) and training data (right) with eddy covariance tower estimates of GPP versus GPP estimated from LUE-NDVI (a - b), LIN-NIR$_v$P (c - d), and LRC-VPD (e - f). The diurnal observations were used for plots a, c, and e. The daily medians of diurnal GPP estimates were used in plots b, d, and f. The black line shows the 1:1 line. The gray line shows the robust regression line.
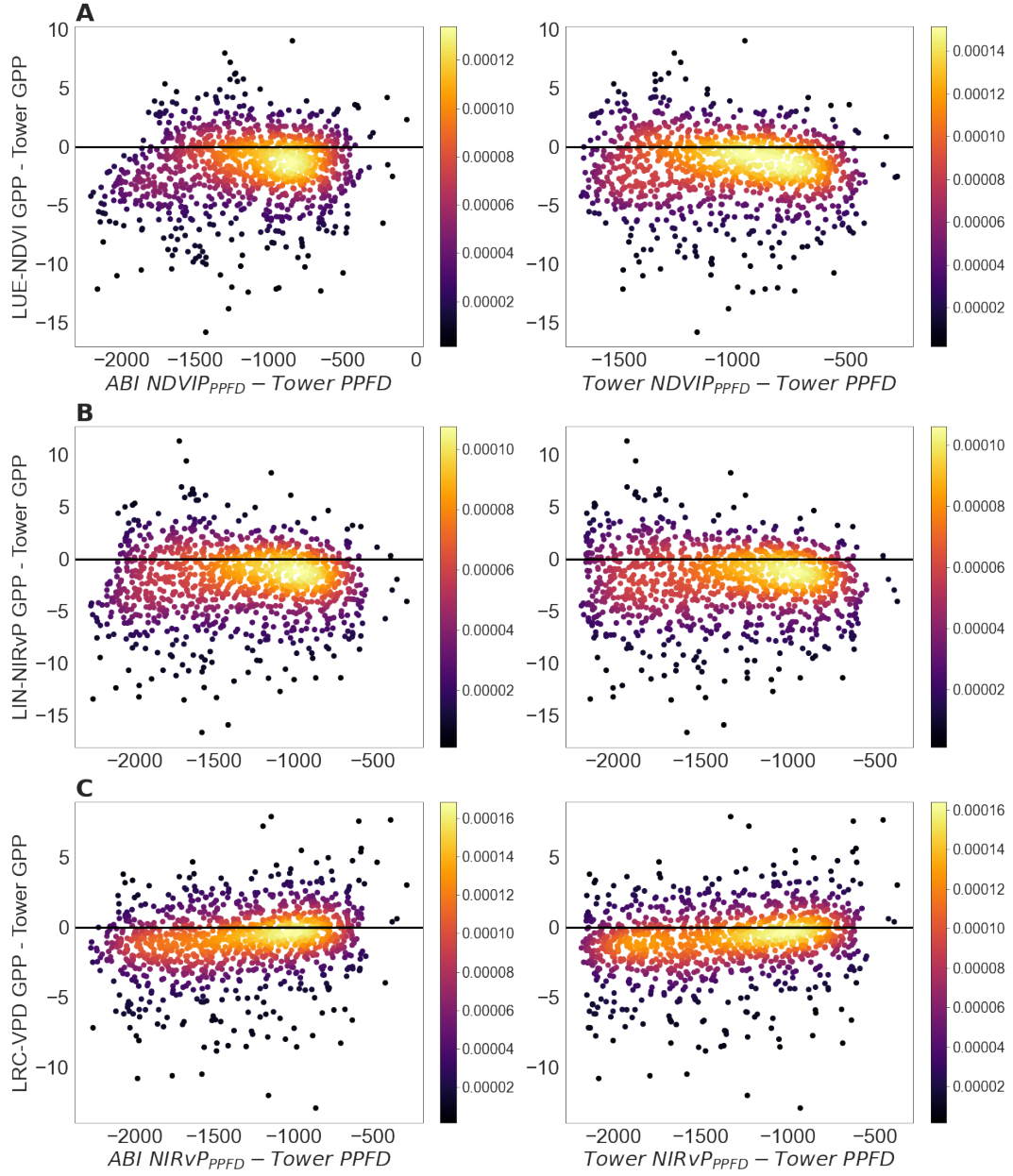
Figure 6: Errors between estimates of GPP vs. difference between $NDVIP_{PPFD}$ and tower incoming photosynthetic photon flux density (PPFD) (A). Errors between estimates of GPP and difference between NIR_vP_{PPFD} and tower incoming photosynthetic photon flux density (PPFD) (B - C). $NDVIP_{PPFD}$ and NIR_vP_{PPFD} calculated from eddy covariance tower NIR_v, NDVI and PPFD are used in the right column. $NDVIP_{PPFD}$ and NIR_vP_{PPFD} calculated from ABI NIR_v, NDVI and ABI PPFD are used in the left column. The units for the x-axis are $\mu mol\,Photons\,m^{-2}\,s^{-1}$ and the units for the y-axis are $\mu mol\,CO_2\,m^{-2}\,s^{-1}$

median C_{GPP}* during the summer months (July - September) with the largest shift of peak GPP in September at a median of 0.41 hours before the peak of incoming solar radiation. GPP estimates from LRC-VPD and LUE-NDVI resulted in the largest median C_{GPP}* during the summer months of July and August in agreement with the EC tower (Figure 7).

The lowest median C_{GPP}* from EC tower estimates occurred during December and January when peak GPP was aligned with the peak of incoming solar radiation (Figure 7). The lowest median C_{GPP}* according to the LRC-VPD estimates also occurred during January (Figure 7). The lowest median C_{GPP}* according to the LUE-NDVI estimates occurred during November (Figure 7). GPP estimates from LIN-NIR$_v$P resulted in very small shifts in peak GPP in relation to incoming short-wave radiation compared to the other GPP estimates throughout the year (Figure 7).

Using tower estimates of GPP, the largest median lag between C_{GPP} and C_{LE} occurred in July when C_{GPP} lagged 0.46 hours before C_{LE} and the smallest median lag occurred in November when median C_{GPP} was aligned with median C_{LE} (Figure 7). GPP estimates from LRC-VPD and LUE-NDVI resulted in the largest median lag between C_{GPP} and C_{LE} during July as well and the smallest median lag during January. Estimates of GPP from the LIN-NIR$_v$P model resulted in the largest median lag between C_{GPP} and C_{LE} during May and the smallest median lag occurred in January (Figure 7).

4 Discussion

4.1 Diurnal environmental stresses

The impact of environmental stresses on GPP at the Tonzi Ranch results from the seasonality in available resources along with the active vegetation type during any given season (grasses vs. tree canopy) (Baldocchi et al., 2004). Below we discuss how the models we tested were able or unable to capture the seasonal shifts from radiation limitation to water limitation on GPP. During the rainy winter, spring, and fall, the Tonzi Ranch receives the lowest global solar radiation and the oak savanna has some of the lowest amounts of net radiation available during this time of the year (Baldocchi et al., 2004). Both the Tonzi Ranch and a nearby Mediterranean grassland is energy limited during the winter rainy season when precipitation exceeds evaporative demand and evaporation is more sensitive to potential evaporation driven by radiation (Baldocchi et al., 2021; Ryu et al., 2008).

The initial light-use efficiency before saturation is reached, α, was lower during the fall, winter and spring months compared to summer. We found the slope between GPP and NIR$_v$P in the LIN-NIR$_v$P model is the highest during the winter and fall months. Furthermore, according to the LUE-NDVI model, the air temperature and VPD stress on maximum LUE was negligible and absorbed radiation tended to be the main control on GPP during the wet winter months (Figure 2). Regardless of each model being able to respond to the increasing radiation limitation during the rainy season, LRC-VPD achieved the highest agreement with EC tower GPP.

As previously discussed, the summer months at the Tonzi Ranch oak savanna are characterized by high incoming solar radiation, declining soil moisture, high air temperatures, and high VPD (Baldocchi et al., 2021). This is also the case for the nearby Vaira grassland which is water-limited during the summer months when high incoming solar radiation increases evaporative demand and evaporation is more sensitive to increases in precipitation (Ryu et al., 2008). At the Tonzi Ranch, low soil moisture can limit summertime ET and the stomatal response of the oak trees to

Figure 7: Difference in diurnal centroids of GPP estimates and incoming shortwave radiation (SW) measured at the eddy covariance tower (C_{GPP}*) (A). Difference in diurnal centroids of GPP estimates and eddy covariance tower latent heat flux (LE) (B). Difference in diurnal centroids of eddy covariance tower GPP and incoming SW, eddy covariance tower LE and incoming SW, and eddy covariance tower VPD and incoming SW (C). Volumetric soil water content at a depth of 0 - 15 cm (D)

.

increasing VPD can serve as an indicator of soil moisture stress (Baldocchi et al., 2021). The best agreement was achieved between tower GPP and LRC-VPD GPP during the water-limited summer through a more accurate specification of the response of GPP to rising VPD during the day. Among the air temperature and VPD stressors of the LUE-NDVI model, the VPD stress on maximum light-use efficiency was the dominant stress on GPP during the summer.

The linear relationship between EC tower GPP and NIR_vP was the least successful in capturing diurnal asymmetry in GPP because it closely follows the course of solar radiation throughout the day and does not capture the impact of increasing diurnal VPD. We found the best agreement between the diurnal centroids of GPP from LIN-NIR_vP and the diurnal centroids of GPP from the EC tower during December and January. These months correspond to the rainy season when radiation can limit GPP and when peak diurnal GPP tended to be aligned with incoming solar radiation. This could explain why these are the only months when LIN-NIR_vP, which only relies on a linear relationship between a potential indicator of absorbed PAR (NIR_vP) and GPP, tended to agree with the diurnal course of GPP. It has been noted that linearities between GPP proxies and GPP are observed at coarse spatiotemporal scales because such scales integrate the structural components and physiological processes (the sun-exposed and shaded leaves on a canopy, the impact of light saturation, etc.) at fine spatiotemporal scales (Anderson et al., 2000; Magney et al., 2020). Our results suggest that fine temporal scales even when the spatial scale is > 1 km could be enough to degrade a linear relationship between GPP and NIR_vP because the impacts of high light and/or other non-linearities driven by micrometerological variation during the day are not captured by linear relationships between GPP and NIR_vP.

4.2 Diurnal dynamics of GPP in relation to soil moisture and evapotranspiration

The shift of the peak of GPP towards the morning hours with progression into the summer months that we found from the LRC-VPD and LUE-NDVI models is consistent with reported shifts in the timing of peak photosynthesis at the Tonzi Ranch (Tang et al., 2005). The peak of photosynthesis at this site has been reported to shift to 9.5 h in July and 9 h during the day in September (Tang et al., 2005). Summertime understory measurements of NEE when the grasses are dead have shown that soil respiration at the Tonzi Ranch peaks during the afternoon in phase with soil temperature during the drought months, while soil respiration under tree cover has shown to peak later than soil temperature (Tang et al., 2005). Soil respiration under the tree has shown to peak 7 - 12 hours after photosynthesis (Tang et al., 2005). The diurnal variation of soil moisture during the summer months is small compared to temperature and photosynthesis which has suggested that both the diurnal variations of tree photosynthesis and soil temperature drive the diurnal variation in soil and stem respiration at the Tonzi Ranch (Tang et al., 2005). In line with EC tower GPP, the increasing shift of GPP towards the morning hours that we found using the light response curve and the LUE model have been previously explained by rising temperatures, increasing R_{eco}, increasing VPD in the afternoon, and stomatal closure during the afternoons at the Tonzi Ranch (Tang et al., 2005).

Seasonally, the peak in surface conductance, GPP, and ET all occur during the rainy spring months after the oak canopy becomes photosynthetically active (Baldocchi et al., 2004, 2021; Ma et al., 2020). During this time LE (λET) tended to peak after incoming SW resulting in larger differences between the peak of EC tower LE and GPP compared to the late summer, fall, and winter months. The light response curve and the LUE model were slightly better at capturing the difference. This indicates that the high surface conductance and soil moisture that

is characteristic of the rainy spring results in the ecosystem being able to respond and maintain LE during high afternoon VPD. On the other hand, the Tonzi Ranch savanna experiences the lowest surface conductance and LE during the dry summer months (Baldocchi et al., 2004). The oak trees also experience a decline in maximum net photosynthesis, maximum carboxylation rate, and maximum electron transport rate with progression into dry season (Xu & Baldocchi, 2003). With volumetric soil water contents below 15%, the ecosystem begins to experience sharp declines in ET/ET$_{equilibrium}$ (Baldocchi et al., 2004). During these months, LE shifts increasingly towards the morning and the differences between the peak of EC tower LE and GPP are some of the smallest. Morning shifts in GPP and ET have been previously identified in Mediteranean/dry climates (Nelson et al., 2018; K. B. Wilson et al., 2003). The ability of the oak trees to access deep ground water resources, their ability to reduce leaf area index, and their ability to regulate water loss allows them to transpire well into the dry summer months possibly maintaining low stomatal conductance or stomatal closure in response to high afternoon VPD (Baldocchi et al., 2021, 2004; Tang et al., 2005). We found that the GPP estimates from the light response curve with a VPD stress and the LUE-NDVI model were best able to follow the increasing alignment of peak GPP and LE with decreasing soil moisture. Consistency between the diurnal (mis)alignment of peak GPP and LE (specifically transpiration, which we did not test) between estimates of GPP from space-based inputs and ecosystem gas-exchange measurements can contribute to understanding when stomatal reactions or non-stomatal reactions are active at large spatial scales (Nelson et al., 2018).

4.3 Uncertainties and moving forward

We found that a light response curve between GPP and NIR$_v$P were able to capture the increasing diurnal asymmetry in GPP at the Tonzi Ranch. Previous research has suggested that the relationship between daily LUE and instantaneous LUE can vary with the time of day during which instantaneous LUE is estimated (Zhang et al., 2018). Midday light saturation could result in instantaneous LUE to be different from estimates of daily LUE (Zhang et al., 2018). However, the light-saturated part of the light response curve is hard to reach at the canopy level because entire canopies include both saturated and unsaturated leaves and space-based sensors capture the integrated response of larger areas that include multiple canopies, shaded leaves, and saturated leaves (Magney et al., 2020). The increasing saturation in the shape of a light response curve that we found during summer can result from high afternoon VPD during conditions of high light and the ecosystem regulating water loss during dry conditions through down regulation of transpiration through stomtal regulation rather than the sole impact of light saturation.

Our analysis of model errors revealed that the light response curves tended to underestimate GPP compared to EC tower GPP when the differences between incident PPFD and NIR$_v$P$_{PPFD}$ are very high. This could mean that LRC-VPD is unable to capture the higher EC tower GPP fluxes because of the light saturation point in LRC-VPD. On the other hand, the error patterns could also arise from the use of NIR$_v$P as a radiation source for GPP and the resulting underestimation of GPP compared to EC tower GPP when there are large difference in incident PPFD and absorbed PPFD. The large differences between NIR$_v$P$_{PPFD}$ and PPFD could occur when the ecosystem receives high PPFD, but NIR$_v$P$_{PPFD}$ could be much lower due to seasonal variations in LAI lowering the estimated GPP. Since this pattern of errors is replicated with the use of NIR$_v$ from tower mounted sensors, the uncertainties associated with atmospheric and angular correction of ABI TOA reflectances, the disagreement between ABI DSR and tower incoming SW, and the conversion of ABI downwelling shortwave radiation to PPFD do not seem to play a major role in these error patterns.

Finally, our atmospheric correction and BRDF correction could have introduced additional uncertainty in NIR_vP estimates. We found that the diurnal shape of NIR_v from our nadir approximation of surface reflectance matched the diurnal shape of NIR_v from the tower mounted sensors at the Tonzi Ranch. However, we did find that magnitude of NIR_v differed between the two sources. This could result from differences in the field of view of the sensors, calibration differences between the sensors, the difference between an albedo-based and reflectance-based NIR_v, or the specification of the atmosphere by 6S in our atmospheric correction. We also used a simple least squares cost function between observed TOA and estimated TOA compared to cost functions that have been previously applied to ABI TOA relflectances which could impact atmospheric and angular correction (He et al., 2019).

Higher-level surface reflectance products from efforts such as the GeoNEX pipeline will be crucial for large scale estimates of GPP from geostaionary satellites (S. Li et al., 2019). Various gap-filling and smoothing techniques need to be tested and developed for very high temporal resolution estimates from geostationary satellites in order to start providing integrated GPP at daily to longer timescales. Diurnal gridded estimates of meteorological variables from reanalysis datasets are also needed for large scale GPP estimates from ABI as have been used for diurnal space-based GPP estimates (X. Li et al., 2021). The response of GPP or R_{eco} to land surface temperature could potentially be used to develop gridded estimates of GPP (X. Li et al., 2021) from ABI with ABI LST being offered hourly. Here, we have tested the use of ABI LST as opposed to VPD as an environmental stress on the maximum CO_2 uptake rate of the light response curve (Appendix A). The resulting GPP estimates result in similar agreement to EC tower GPP compared to the LRC-VPD estimates (Figure A2).

The approaches of partitioning NEE into GPP and ecosystem respiration can impact both fluxes (Lasslop et al., 2010; Stoy et al., 2006) and therefore, future studies that evaluate the use of multiple partitioning approaches for estimating GPP from remotely sensed inputs could be insightful. Here, we tested all three models with GPP partitioned using approaches that rely on nighttime data alone and both nighttime and daytime data (Appendix B). Using the LRC-VPD and LUE-NDVI, we found better agreement between GPP estimates and EC tower GPP using the Lasslop et al. (2010) approach that relies on both daytime and nighttime NEE data (Figure B1 - B2). The better agreement between LRC-VPD GPP estimates and the Lasslop et al. (2010) partitioned GPP is obvious since they both rely on the same underlying assumptions for the response of GPP to light and the VPD stress on GPP.

Coupled carbon-water-energy dynamics could in principle be studied by estimating GPP using the Atmosphere-Land Exchange Inverse (ALEXI) model which is already used to estimate ET using GOES. In other words, there are opportunities to couple carbon and water fluxes using ABI observations that may improve our understanding of both (Anderson et al., 2000, 2008). Finally, it has been suggested that plant strategies for regulating water loss through stomatal regulation in the face of drops in soil water potential can impact how sensitive plant productivity is to VPD or precipitation (Konings, Williams, & Gentine, 2017). Ecosystem water regulation strategies can be characterized on a continuum of isohydricity to anisohydricity based on both ground-based and space-based measurements (Konings & Gentine, 2017; Novick et al., 2019). ABI based diurnal GPP estimates can help us investigate how quickly ecosystem carbon uptake is responding to water stress through diurnal shifts in GPP according to ecosystem water regulation strategies (Nelson et al., 2018) and the agreement in these dynamics between ground and space-based estimates.

5 Conclusion

Diurnal estimates of GPP from geostationary satellites can provide us with observation-based estimates of GPP at very high temporal resolutions for studying diurnal dynamics at large scales. They can provide GPP estimates integrated at daily to longer timescales for intercomparison studies and provide near-real time estimates of GPP. Half-hour space-based estimates are also comparable to the timescale at which ecosystem gas exchange measurements from eddy covariance towers are reported. We tested three widely-used models to estimate GPP with 5-minute inputs from the Advanced Baseline Imager on the GOES-R series in an oak savanna ecosystem that experiences seasonal moisture stress and shifts in resource limitations throughout the year. We found that a light response curve with a proper VPD stress is in best agreement with ground-based ecosystem gas exchange measurements about the increasing diurnal asymmetry in GPP the ecosystem experiences during the dry summer season. We also found that GPP estimated with the light response curve is in best agreement with ground estimates during all other seasons highlighting the flexibility of the light response curve with proper environmental stresses for diurnal estimates. However, we did find that the the light saturation point from light response curves underestimated GPP compared to GPP partitioned from gas exchange measurements during times of high incoming photosynthetic photon flux density. We found that linearities between NIR_vP and GPP appear to break down at the diurnal scale due to stomatal and non-stomatal responses to changing irradiance and other environmental variables during the day. Finally, we found that GPP estimates from light response curves with a VPD stress and light-use efficiency models are in best agreement with the diurnal (mis)alignment of GPP and latent heat exchange in response to diurnal environmental variation. This agreement can be important for studying diurnal water-use efficiency and disentangling diurnal stomatal and non-stomtal responses to environmental stresses. Moving forward to estimating diurnal ABI based GPP at other ecosystems with eddy covariance towers, we find that it is important to test multiple GPP model forms at the diurnal scale to understand how seasonal resource availability and environmental conditions impact the diurnal GPP estimates. Surface reflectance and angular corrected reflectances could greatly facilitate the development of diurnal GPP estimates from remotely sensed inputs at regional to hemispheric scales.

Appendix A Land surface temperature stress on maximum CO_2 uptake rate in the light response curve

To test an LST stress on GPP, the light response curve of equation 13 was modified with GOES-R ABI LST (ABI-L2-LSTC) as an input. Similar to ABI DSR, we linearly interpolated the hourly ABI LST to half hour time steps to match the data from eddy covariance tower. Using a light response curve similar to Lasslop et al. (2010), GPP was estimated as:

$$GPP = \frac{\alpha_{LST} \, NIR_vP \, \beta_{LST}}{\beta_{LST} + \alpha_{LST} \, NIR_vP} \tag{A1}$$

where α_{LST} is the canopy LUE before light saturation is reached ($\mu mol \, CO_2 \, J^{-1}$) or the initial slope of the relationship between GPP and NIR_vP and β_{LST} is the maximum CO_2 uptake rate at the point of light saturation ($\mu mol \, CO_2 \, m^{-2} \, s^{-1}$). The impact of increasing LST and the resulting stress on the maximum CO_2 uptake rate at light saturation, β_{LST}, was estimated as:

$$\beta_{LST} = \frac{\beta_{0_{LST}}}{1 + exp(-b \times (LST - LST_0))} \tag{A2}$$

Table A1: Comparison of mean error (ME), mean absolute error (MAE), and normalized MAE (NMAE) between ABI based GPP estimates and eddy covriance tower GPP estimates. The units for ME and MAE are $\mu mol\, CO_2\, m^{-2}\, s^{-1}$.

	Training data			Test data		
Season	**ME**	**MAE**	**NMAE**	**ME**	**MAE**	**NMAE**
Winter	−0.262	1.844	0.319	−0.302	1.914	0.325
Spring	−0.293	2.694	**0.280**	−0.260	2.582	**0.275**
Summer	**−0.177**	1.708	0.443	−0.187	1.700	0.447
Fall	−0.281	**1.363**	0.452	**−0.153**	**1.450**	0.498

740 where $\beta_{0_{LST}}$ is the maximum CO_2 uptake rate at light saturation during condi-
741 tions of ideal LST. The parameters α_{LST}, $\beta_{0_{LST}}$, b, and LST_0 were optimized using
742 EC tower GPP as described in equations 15 and 16 from section 2.3.

743 The lowest training mean error was achieved during the summer (-0.18) and
744 the lowest testing mean error was achieved during the fall (-0.15). The lowest train-
745 ing and testing normalized mean absolute error were achieved during the spring
746 (0.28) (Table A1). The error summaries are some of the lowest among all the models
747 and are comparable to LRC-VPD (Table 2). Similarly, the linear relationship from
748 a robust regression between GPP estimated from LRC-LST and EC tower GPP
749 (Figure A1) was similar to the linear relationships between GPP estimated from
750 the other three models and EC tower GPP (Figure 6). The diurnal means of GPP
751 from LRC-LST were also most in agreement with EC tower GPP and LRC-VPD
752 throughout the year (Figure A2). The disagreement between specifying an LST or
753 VPD stress on the maximum CO_2 uptake rate was most evident during summer
754 late afternoon - early evening. As LST began to decrease in the early evening hours,
755 LRC-LST GPP increased which was not in agreement with GPP partitioned at the
756 EC tower.

Appendix B Comparison of NEE partitioning approaches

758 To test the impact of different EC tower NEE partitioning approaches on GPP
759 estimates with ABI inputs, we tested optimizing the parameters of LRC-VPD, LUE-
760 NDVI, and LIN-NIR$_v$P with two different EC tower GPP estimates from partition-
761 ing NEE using REddyProc (Wutzler et al., 2018). The first method has no explicit
762 assumptions about the response of GPP to light and only uses nighttime data to
763 estimate a temporally varying respiration-temperature relationship for vegetation
764 that does not utilize Crassulacean acid metabolism as (Reichstein et al., 2005):

$$R_{eco}(T) = R_{Ref}\, exp[E_0(\frac{1}{T_{Ref} - T_0} - \frac{1}{T - T_0})] \tag{B1}$$

766 where T is air temperature $°C$, E_0 is the temperature sensitivity, T_0 is held
767 constant at $-46.02°C$, and T_{Ref} is held at $15°C$ (Reichstein et al., 2005; Wutzler et
768 al., 2018). E_0 is estimated using 15-day windows of nighttime data and the short-
769 term E_0 estimates are aggregated to an annual value (Reichstein et al., 2005; Wut-
770 zler et al., 2018). Using the annual E_0 estimate, the R_{Ref} parameter is estimated
771 with 7-day windows that are shifted for 4 days. The resulting R_{Ref} is assigned to
772 the central time point of the 4 days and linearly interpolated between estimates
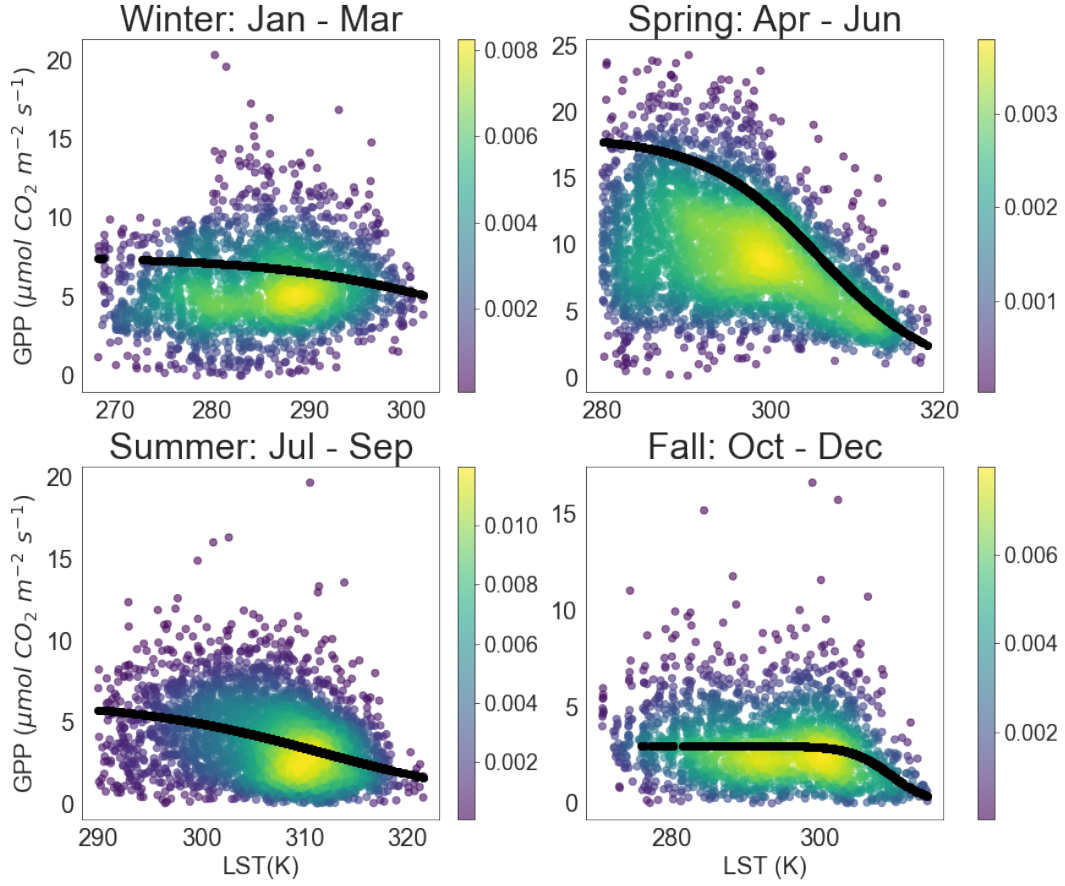
Figure A1: The response of eddy covariance tower GPP to land surface temperature (LST). The black lines shows the values of β_{LST} estimated using equation A2.
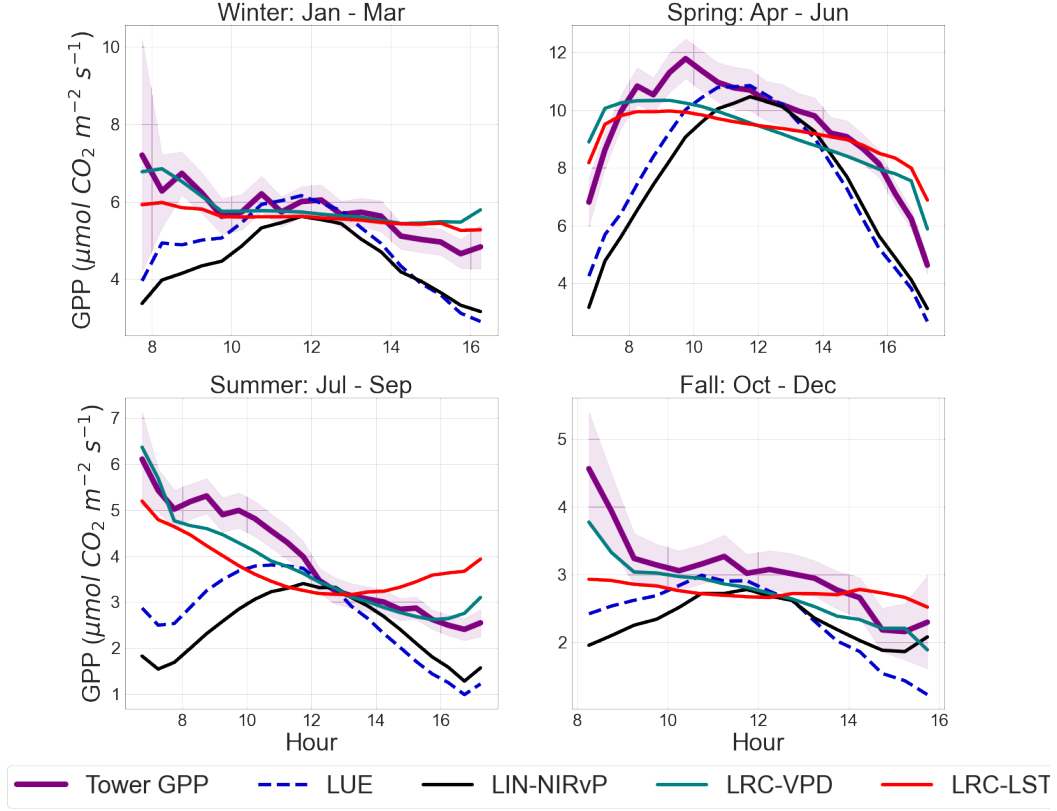
Figure A2: Seasonal diurnal means of estimates of GPP from the all models and diurnal means of estimates of GPP from the eddy covariance tower. The purple shaded region shows ±2 standard error of mean eddy covariance tower GPP. The data spans from Jan 2019 - Dec 2020.
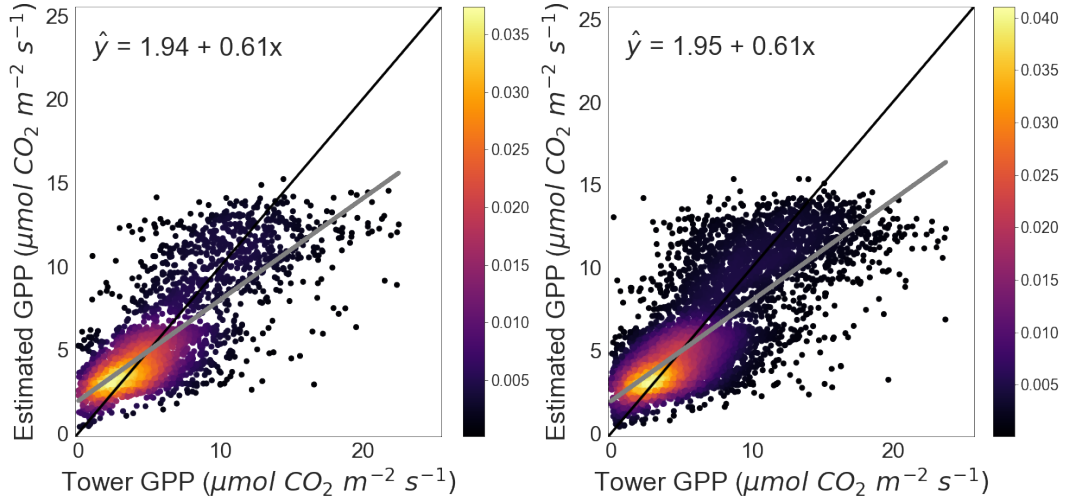

Figure A3: Scatter plots of test data (left) and training data (right) with eddy covariance tower estimates of GPP versus GPP estimated from LRC-LST. The black line shows the 1:1 line and the gray line shows the robust regression line.

773 (Reichstein et al., 2005; Wutzler et al., 2018). The R_{eco} and air temperature rela-
774 tionship is extrapolated to daytime data to obtain estimates of R_{eco} during the day.
775 Finally, R_{eco} estimates are used to estimate GPP as (Reichstein et al., 2005; Wutzler
776 et al., 2018):

$$GPP = R_{eco} - NEE \tag{B2}$$

778 The second method includes a daytime light response function for GPP along
779 with the response of R_{eco} to air temperature and uses both nighttime data and
780 daytime data to estimate NEE as (Lasslop et al., 2010; Wutzler et al., 2018):

$$NEE = \frac{\alpha \beta R_g}{\alpha R_g + \beta} + \gamma \tag{B3}$$

$$= \frac{\alpha \beta R_g}{\alpha R_g + \beta} + R_{Ref} \, exp[E_0(\frac{1}{T_{Ref} - T_0} - \frac{1}{T - T_0})] \tag{B4}$$

784 where α is the canopy LUE before light saturation is reached ($\mu mol\, CO_2\, J^{-1}$)
785 and β is the maximum CO_2 uptake rate at the point of light saturation
786 ($\mu mol\, CO_2\, m^{-2}\, s^{-1}$), R_g is incoming shortwave radiation at the surface of the
787 Earth, and $\gamma\, (\mu mol\, CO_2\, m^{-2}\, s^{-1})$ is R_{eco}. The impact of increasing VPD and
788 the resulting stress on the maximum CO_2 uptake rate at light saturation, β, was
789 estimated according to Lasslop et al. (2010) using equation 14. T_0 is fixed ac-
790 cording to the nighttime partitioning (Wutzler et al., 2018). T_{Ref} is fixed within
791 moving windows to the median temperature in the window and E_0 is estimated
792 from nighttime data for windows shifted by 2 days (Wutzler et al., 2018). E_0 es-
793 timates are smoothed and a prior R_{Ref} is estimated from nighttime data for each
794 window (Wutzler et al., 2018). Finally, the parameters of the light response curve
795 $(R_{Ref}, \alpha, \beta_0, k)$ are estimated using daytime data for each window (Wutzler et al.,
796 2018).

797 Both nighttime and daytime partitioning methods resulted in similar relation-
798 ships with GPP estimates from ABI inputs using both diurnal observations and
799 daily medians (Figure B1 and B2). Daytime partitioning resulted in relationships
800 between diurnal EC tower GPP and LRC-VPD and LUE-NDVI GPP estimates that
801 were slightly closer to a 1:1 line compared to nighttime partitioning (Figure B1 and
802 B2). The slightly better linear relationship between GPP estimated from daytime
803 partitioning and from LRC-VPD is expected considering that both GPP estimates
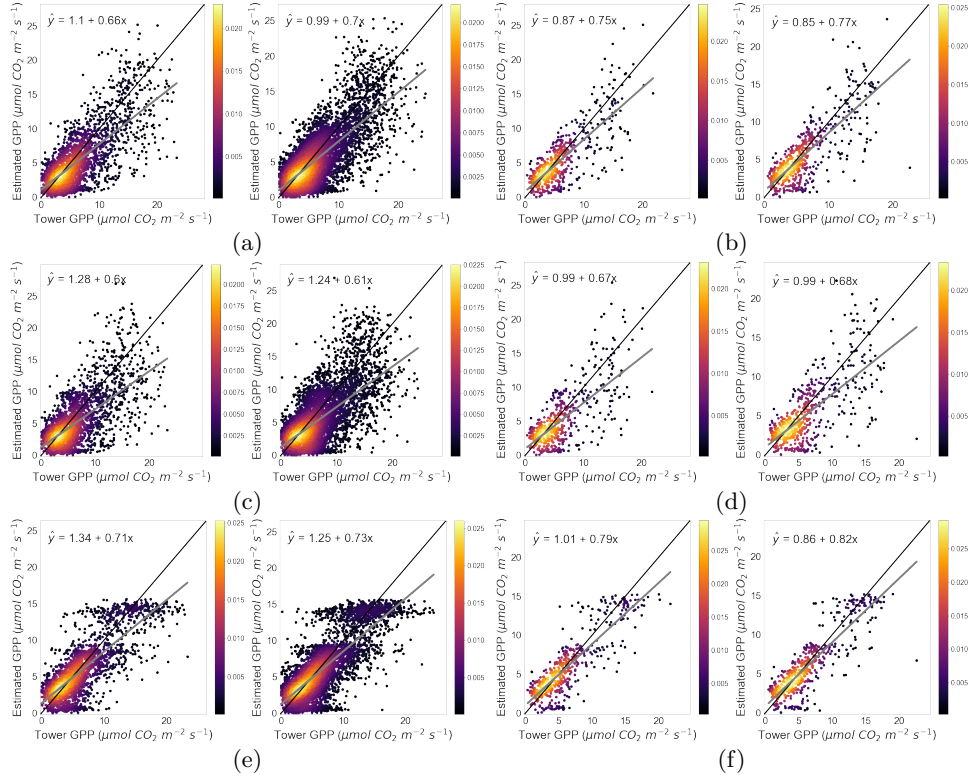804 are derived from the same equations as outlined by Lasslop et al. (2010).

Figure B1: For each pair of plots a - f, scatter plots of test data (left) and training data (right) with eddy covariance tower estimates of GPP using the NEE partitioning approach based on nighttime NEE data versus GPP estimated from LUE-NDVI (a - b), LIN-NIR$_v$P (c - d), and LRC-VPD (e - f). The diurnal observations were used for plots a, c, and e. The daily medians of diurnal GPP estimates were used in plots b, d, and f. The black line shows the 1:1 line. The gray line shows the robust regression line.
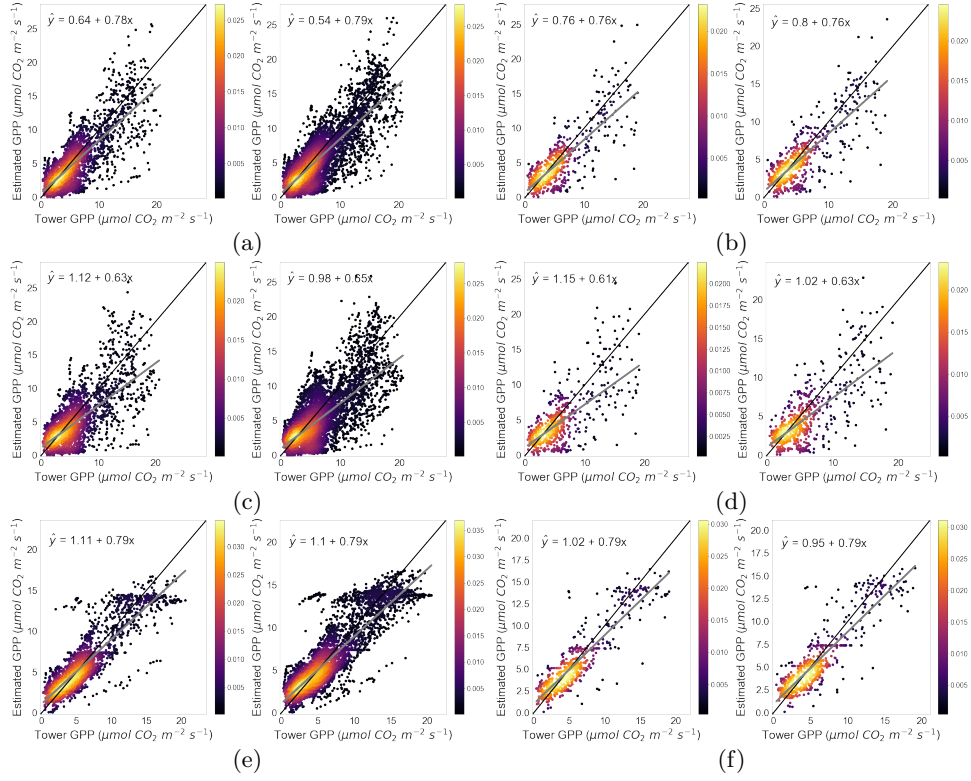
Figure B2: For each pair of plots a - f, scatter plots of test data (left) and training data (right) with eddy covariance tower estimates of GPP using the NEE partitioning approach based on nighttime and daytime NEE data versus GPP estimated from LUE-NDVI (a - b), LIN-NIR$_v$P (c - d), and LRC-VPD (e - f). The diurnal observations were used for plots a, c, and e. The daily medians of diurnal GPP estimates were used in plots b, d, and f. The black line shows the 1:1 line. The gray line shows the robust regression line.

References

Anav, A., Friedlingstein, P., Beer, C., Ciais, P., Harper, A., Jones, C., . . . Zhao, M.
    (2015).   Spatiotemporal patterns of terrestrial gross primary production: A
    review. *Reviews of Geophysics*, *53*(3), 785–818. doi: 10.1002/2015RG000483

Anderson, M. C., Norman, J. M., Kustas, W. P., Houborg, R., Starks, P. J., &
    Agam, N.   (2008).   A thermal-based remote sensing technique for routine
    mapping of land-surface carbon, water and energy fluxes from field to re-
    gional scales.   *Remote Sensing of Environment*, *112*(12), 4227–4241.   doi:
    10.1016/j.rse.2008.07.009

Anderson, M. C., Norman, J. M., Meyers, T. P., & Diak, G. R.   (2000).   An analyt-
    ical model for estimating canopy transpiration and carbon assimilation fluxes
    based on canopy light-use efficiency.   *Agricultural and Forest Meteorology*,
    101(4), 265–289. doi: 10.1016/S0168-1923(99)00170-7

Badgley, G., Anderegg, L. D. L., Berry, J. A., & Field, C. B.   (2019).   Terrestrial
    gross primary production: Using NIRV to scale from site to globe.   *Global
    Change Biology*, *25*(11), 3731–3740. doi: 10.1111/gcb.14729

Badgley, G., Field, C. B., & Berry, J. A.   (2017).   Canopy near-infrared reflectance
    and terrestrial photosynthesis.   *Science Advances*, *3*(3), e1602244.   doi: 10
    .1126/sciadv.1602244

Baldocchi, D.   (1997).   Measuring and modelling carbon dioxide and water
    vapour exchange over a temperate broad-leaved forest during the 1995
    summer drought.   *Plant, Cell & Environment*, *20*(9), 1108–1122.   doi:
    10.1046/j.1365-3040.1997.d01-147.x

Baldocchi, D., Ma, S., & Verfaillie, J.   (2021).   On the inter- and intra-annual vari-
    ability of ecosystem evapotranspiration and water use efficiency of an oak
    savanna and annual grassland subjected to booms and busts in rainfall.   *Global
    Change Biology*, *27*(2). doi: https://doi.org/10.1111/gcb.15414

Baldocchi, D., Ryu, Y., Dechant, B., Eichelmann, E., Hemes, K., Ma, S., . . . Berry,
    J. A.   (2020).   Outgoing near infrared radiation from vegetation scales with
    canopy photosynthesis across a spectrum of function, structure, physiological
    capacity and weather.   *Journal of Geophysical Research: Biogeosciences*.   doi:
    10.1029/2019JG005534

Baldocchi, D., Xu, L., & Kiang, N.   (2004).   How plant functional-type, weather,
    seasonal drought, and soil physical properties alter water and energy fluxes
    of an oak–grass savanna and an annual grassland.   *Agricultural and Forest
    Meteorology*, *123*(1), 13–39. doi: 10.1016/j.agrformet.2003.11.006

Beer, C., Reichstein, M., Tomelleri, E., Ciais, P., Jung, M., Carvalhais, N., . . .
    Papale, D.   (2010).   Terrestrial gross carbon dioxide uptake: Global dis-

tribution and covariation with climate. *Science*, *329*(5993), 834–838. doi: 10.1126/science.1184984

Bucci, S. J., Silletta, L. M. C., Garré, A., Cavallaro, A., Efron, S. T., Arias, N. S., ... Scholz, F. G. (2019). Functional relationships between hydraulic traits and the timing of diurnal depression of photosynthesis. *Plant, Cell & Environment*, *42*(5), 1603–1614. doi: https://doi.org/10.1111/pce.13512

Chen, M., Rafique, R., Asrar, G. R., Bond-Lamberty, B., Ciais, P., Zhao, F., ... Hickler, T. (2017). Regional contribution to variability and trends of global gross primary productivity. *Environmental Research Letters*, *12*(10), 105005. doi: 10.1088/1748-9326/aa8978

Chen, X., Rubin, Y., Ma, S., & Baldocchi, D. (2008). Observations and stochastic modeling of soil moisture control on evapotranspiration in a Californian oak savanna. *Water Resources Research*, *44*(8). doi: https://doi.org/10.1029/2007WR006646

Chu, H., Luo, X., Ouyang, Z., Chan, W. S., Dengel, S., Biraud, S. C., ... Zona, D. (2021). Representativeness of Eddy-Covariance flux footprints for areas surrounding AmeriFlux sites. *Agricultural and Forest Meteorology*, *301-302*. doi: 10.1016/j.agrformet.2021.108350

Cowan, I., & Farquhar, G. (1977). Stomatal function in relation to leaf metabolism and environment: Stomatal function in the regulation of gas exchange. *Symposia of the Society for Experimental Biology*, *31*, 471–505.

Cramer, W., Kicklighter, D. W., Bondeau, A., Iii, B. M., Churkina, G., Nemry, B., ... of The Potsdam NPP Model Intercomparison, T. P. (1999). Comparing global models of terrestrial net primary productivity (NPP): overview and key results. *Global Change Biology*, *5*(S1), 1–15. doi: 10.1046/j.1365-2486.1999.00009.x

Dechant, B., Ryu, Y., Badgley, G., Köhler, P., Rascher, U., Migliavacca, M., ... Berry, J. A. (2020). NIRvP: a robust structural proxy for sun-induced chlorophyll fluorescence and photosynthesis across scales. *EarthArXiv [preprint]*. Retrieved from `https://eartharxiv.org/repository/view/1936/`

Desai, A. R., Noormets, A., Bolstad, P. V., Chen, J., Cook, B. D., Davis, K. J., ... Wang, W. (2008). Influence of vegetation and seasonal forcing on carbon dioxide fluxes across the upper midwest, USA: Implications for regional scaling. *Agricultural and Forest Meteorology*, *148*(2), 288–308. doi: 10.1016/j.agrformet.2007.08.001

Field, C. B., Randerson, J. T., & Malmström, C. M. (1995). Global net primary production: Combining ecology and remote sensing. *Remote Sensing of Environment*, *51*(1), 74–88. doi: 10.1016/0034-4257(94)00066-V

Grossiord, C., Buckley, T. N., Cernusak, L. A., Novick, K. A., Poulter, B., Siegwolf, R. T. W., ... McDowell, N. G. (2020). Plant responses to rising vapor pressure deficit. *New Phytologist*, *226*(6), 1550–1566. doi: https://doi.org/10.1111/nph.16485

Gu, L., Baldocchi, D., Verma, S. B., Black, T. A., Vesala, T., Falge, E. M., & Dowty, P. R. (2002). Advantages of diffuse radiation for terrestrial ecosystem productivity. *Journal of Geophysical Research: Atmospheres*, *107*, ACL 2–1–ACL 2–23. doi: 10.1029/2001JD001242

He, T., Liang, S., Wang, D., Wu, H., Yu, Y., & Wang, J. (2012). Estimation of surface albedo and directional reflectance from Moderate Resolution Imaging Spectroradiometer (MODIS) observations. *Remote Sensing of Environment*, *119*. doi: 10.1016/j.rse.2012.01.004

He, T., Zhang, Y., Liang, S., Yu, Y., & Wang, D. (2019). Developing land surface directional reflectance and albedo products from geostationary GOES-R and himawari data: Theoretical basis, operational implementation, and validation. *Remote Sensing*, *11*(22), 2655. doi: 10.3390/rs11222655

Huang, X., Xiao, J., Wang, X., & Ma, M. (2021). Improving the global MODIS

GPP model by optimizing parameters with FLUXNET data. *Agricultural and Forest Meteorology*, *300*, 108314. doi: 10.1016/j.agrformet.2020.108314

Jalakas, P., Takahashi, Y., Waadt, R., Schroeder, J. I., & Merilo, E. (2021). Molecular mechanisms of stomatal closure in response to rising vapour pressure deficit. *New Phytologist*. doi: 10.1111/nph.17592

Joiner, J., & Yoshida, Y. (2020). Satellite-based reflectances capture large fraction of variability in global gross primary production (GPP) at weekly time scales. *Agricultural and Forest Meteorology*, *291*, 108092. doi: 10.1016/j.agrformet.2020.108092

Joiner, J., Yoshida, Y., Zhang, Y., Duveiller, G., Jung, M., Lyapustin, A., ... Tucker, C. J. (2018). Estimation of Terrestrial Global Gross Primary Production (GPP) with Satellite Data-Driven Models and Eddy Covariance Flux Data. *Remote Sensing*, *10*(9), 1346. doi: 10.3390/rs10091346

Jung, M., Schwalm, C., Migliavacca, M., Walther, S., Camps-Valls, G., Koirala, S., ... Reichstein, M. (2020). Scaling carbon fluxes from eddy covariance sites to globe: synthesis and evaluation of the FLUXCOM approach. *Biogeosciences*, *17*(5), 1343–1365. doi: https://doi.org/10.5194/bg-17-1343-2020

Kannenberg, S. A., Bowling, D. R., & Anderegg, W. R. L. (2020). Hot moments in ecosystem fluxes: High GPP anomalies exert outsized influence on the carbon cycle and are differentially driven by moisture availability across biomes. *Environmental Research Letters*, *15*(5), 054004. doi: 10.1088/1748-9326/ab7b97

Keenan, T. F., Baker, I., Barr, A., Ciais, P., Davis, K., Dietze, M., ... Richardson, A. D. (2012). Terrestrial biosphere model performance for inter-annual variability of land-atmosphere CO_2 exchange. *Global Change Biology*, *18*(6), 1971–1987. doi: 10.1111/j.1365-2486.2012.02678.x

Khan, A. M., Stoy, P. C., Douglas, J. T., Anderson, M., Diak, G., Otkin, J. A., ... McCorkel, J. (2021). Reviews and syntheses: Ongoing and emerging opportunities to improve environmental science using observations from the Advanced Baseline Imager on the Geostationary Operational Environmental Satellites. *Biogeosciences*, *18*(13), 4117–4141. doi: 10.5194/bg-18-4117-2021

Konings, A. G., & Gentine, P. (2017). Global variations in ecosystem-scale isohydricity. *Global Change Biology*, *23*(2), 891–905. doi: 10.1111/gcb.13389

Konings, A. G., Williams, A. P., & Gentine, P. (2017). Sensitivity of grassland productivity to aridity controlled by stomatal and xylem regulation. *Nature Geoscience*, *10*(4), 284–288. doi: 10.1038/ngeo2903

Konings, A. G., Yu, Y., Xu, L., Yang, Y., Schimel, D. S., & Saatchi, S. S. (2017). Active microwave observations of diurnal and seasonal variations of canopy water content across the humid African tropical forests. *Geophysical Research Letters*, *44*(5), 2290–2299. doi: https://doi.org/10.1002/2016GL072388

Lasslop, G., Reichstein, M., Papale, D., Richardson, A. D., Arneth, A., Barr, A., ... Wohlfahrt, G. (2010). Separation of net ecosystem exchange into assimilation and respiration using a light response curve approach: critical issues and global evaluation. *Global Change Biology*, *16*(1), 187–208. doi: https://doi.org/10.1111/j.1365-2486.2009.02041.x

Lawson, T. (2009). Guard cell photosynthesis and stomatal function. *New Phytologist*, *181*(1), 13–34. doi: 10.1111/j.1469-8137.2008.02685.x

Li, S., Wang, W., Hashimoto, H., Xiong, J., Vandal, T., Yao, J., ... Nemani, R. (2019). First Provisional Land Surface Reflectance Product from Geostationary Satellite Himawari-8 AHI. *Remote Sensing*, *11*(24). doi: 10.3390/rs11242990

Li, X., Xiao, J., Fisher, J. B., & Baldocchi, D. (2021). ECOSTRESS estimates gross primary production with fine spatial resolution for different times of day from the International Space Station. *Remote Sensing of Environment*, *258*, 112360. doi: 10.1016/j.rse.2021.112360

Lin, C., Gentine, P., Frankenberg, C., Zhou, S., Kennedy, D., & Li, X. (2019). Evaluation and mechanism exploration of the diurnal hysteresis of ecosys-

tem fluxes. *Agricultural and Forest Meteorology*, *278*, 107642. doi: 10.1016/j.agrformet.2019.107642

Ma, S., Baldocchi, D., Wolf, S., & Verfaillie, J. (2016). Slow ecosystem responses conditionally regulate annual carbon balance over 15 years in Californian oak-grass savanna. *Agricultural and Forest Meteorology*, *228-229*, 252–264. doi: 10.1016/j.agrformet.2016.07.016

Ma, S., Eichelmann, E., Wolf, S., Rey-Sanchez, C., & Baldocchi, D. D. (2020). Transpiration and evaporation in a Californian oak-grass savanna: Field measurements and partitioning model results. *Agricultural and Forest Meteorology*, *295*, 108204. doi: 10.1016/j.agrformet.2020.108204

Ma, S., Xu, L., Verfaillie, J., & Baldocchi, D. (2001). *Ameriflux US-Ton Tonzi Ranch, Dataset.* Retrieved from `https://doi.org/10.17190/AMF/1245971`

Magney, T. S., Barnes, M. L., & Yang, X. (2020). On the Covariation of Chlorophyll Fluorescence and Photosynthesis Across Scales. *Geophysical Research Letters*, *47*(23), e2020GL091098. doi: 10.1029/2020GL091098

Mahadevan, P., Wofsy, S. C., Matross, D. M., Xiao, X., Dunn, A. L., Lin, J. C., . . . Gottlieb, E. W. (2008). A satellite-based biosphere parameterization for net ecosystem CO_2 exchange: Vegetation Photosynthesis and Respiration Model (VPRM): NET ECOSYSTEM EXCHANGE MODEL. *Global Biogeochemical Cycles*, *22*(2). doi: 10.1029/2006GB002735

Matheny, A. M., Bohrer, G., Stoy, P. C., Baker, I. T., Black, A. T., Desai, A. R., . . . Verbeeck, H. (2014). Characterizing the diurnal patterns of errors in the prediction of evapotranspiration by several land-surface models: An NACP analysis. *Journal of Geophysical Research: Biogeosciences*, *119*(7), 1458–1473. doi: https://doi.org/10.1002/2014JG002623

Matthews, J. S. A., Vialet-Chabrand, S. R. M., & Lawson, T. (2017). Diurnal variation in gas exchange: The balance between carbon fixation and water loss. *Plant Physiology*, *174*(2), 614–623. doi: 10.1104/pp.17.00152

Meek, D. W., Hatfield, J. L., Howell, T. A., Idso, S. B., & Reginato, R. J. (1984). A generalized relationship between Photosynthetically Active Radiation and solar radiation. *Agronomy Journal*, *76*(6), 939–945. doi: 10.2134/agronj1984.00021962007600060018x

Meinzer, F. C., Smith, D. D., Woodruff, D. R., Marias, D. E., McCulloh, K. A., Howard, A. R., & Magedman, A. L. (2017). Stomatal kinetics and photosynthetic gas exchange along a continuum of isohydric to anisohydric regulation of plant water status. *Plant, Cell & Environment*, *40*(8), 1618–1628. doi: https://doi.org/10.1111/pce.12970

Merrick, T., Pau, S., Detto, M., Broadbent, E. N., Bohlman, S., Still, C. J., & Almeyda Zambrano, A. M. (2021). Unveiling spatial and temporal heterogeneity of a tropical forest canopy using high-resolution NIRv, FCVI, and NIRvrad from UAS observations. *Biogeosciences Discussions [preprint]*, 1–20. doi: 10.5194/bg-2021-95

NASA, D. . N. . N. . (2018). GOES-R Advanced Baseline Imager (ABI) Algorithm Theoretical Basis Document For Downward Shortwave Radiation (Surface), and Reflected Shortwave Radiation (TOA) [Computer software manual]. Retrieved from `https://www.goes-r.gov/users/docs/PUG-L1b-vol3.pdf`

NASA, D. . N. . N. . (2019). Product Definition and User's Guide (PUG): Volume 3: Level 1b Products [Computer software manual]. Retrieved from `https://www.goes-r.gov/users/docs/PUG-L1b-vol3.pdf`

Nelson, J. A., Carvalhais, N., Migliavacca, M., Reichstein, M., & Jung, M. (2018). Water-stress-induced breakdown of carbon–water relations: indicators from diurnal FLUXNET patterns. *Biogeosciences*, *15*(8), 2433–2447. doi: https://doi.org/10.5194/bg-15-2433-2018

Novick, K. A., Ficklin, D. L., Stoy, P. C., Williams, C. A., Bohrer, G., Oishi, A. C., . . . Phillips, R. P. (2016). The increasing importance of atmospheric de-

mand for ecosystem water and carbon fluxes. *Nature Climate Change*, *6*(11), 1023–1027. doi: 10.1038/nclimate3114

Novick, K. A., Konings, A. G., & Gentine, P. (2019). Beyond soil water potential: An expanded view on isohydricity including land–atmosphere interactions and phenology. *Plant, Cell & Environment*, *42*(6), 1802–1815. doi: https://doi.org/10.1111/pce.13517

O'Sullivan, M., Smith, W. K., Sitch, S., Friedlingstein, P., Arora, V. K., Haverd, V., . . . Buermann, W. (2020). Climate-Driven Variability and Trends in Plant Productivity Over Recent Decades Based on Three Global Products. *Global Biogeochemical Cycles*, *34*(12), e2020GB006613. doi: 10.1029/2020GB006613

Pedregosa, F., Varoquaux, G., Gramfort, A., Michel, V., Thirion, B., Grisel, O., . . . Duchesnay, E. (2011). Scikit-learn: Machine learning in Python. *Journal of Machine Learning Research*, *12*, 2825–2830.

Prince, S. D., & Goward, S. N. (1995). Global Primary Production: A Remote Sensing Approach. *Journal of Biogeography*, *22*(4/5), 815–835. doi: 10.2307/2845983

Qin, W., Herman, J. R., & Ahmad, Z. (2001). A fast, accurate algorithm to account for non-lambertian surface effects on TOA radiance. *Journal of Geophysical Research: Atmospheres*, *106*, 22671–22684. doi: 10.1029/2001JD900215

Randazzo, N. A., Michalak, A. M., & Desai, A. R. (2020). Synoptic Meteorology Explains Temperate Forest Carbon Uptake. *Journal of Geophysical Research: Biogeosciences*, *125*(2), e2019JG005476. doi: 10.1029/2019JG005476

Reichstein, M., Falge, E., Baldocchi, D., Papale, D., Aubinet, M., Berbigier, P., . . . Valentini, R. (2005). On the separation of net ecosystem exchange into assimilation and ecosystem respiration: review and improved algorithm. *Global Change Biology*, *11*(9), 1424–1439. Retrieved from `http://onlinelibrary.wiley.com/doi/abs/10.1111/j.1365-2486.2005.001002.x` doi: 10.1111/j.1365-2486.2005.001002.x

Reichstein, M., Stoy, P. C., Desai, A. R., Lasslop, G., & Richardson, A. D. (2012). Partitioning of net fluxes. In M. Aubinet, T. Vesala, & D. Papale (Eds.), *Eddy covariance* (pp. 263–289). Springer Netherlands. doi: 10.1007/978-94-007-2351-1_9

Roby, M. C., Scott, R. L., & Moore, D. J. P. (2020). High vapor pressure deficit decreases the productivity and water-use efficiency of rain-induced pulses in semiarid ecosystems. *Journal of Geophysical Research: Biogeosciences*, e2020JG005665. Retrieved from `http://agupubs.onlinelibrary.wiley.com/doi/abs/10.1029/2020JG005665` doi: 10.1029/2020JG005665

Ruimy, A., Dedieu, G., & Saugier, B. (1996). TURC: A diagnostic model of continental gross primary productivity and net primary productivity. *Global Biogeochemical Cycles*, *10*(2), 269–285. doi: 10.1029/96GB00349

Running, S. W., Nemani, R. R., Heinsch, F. A., Zhao, M., Reeves, M., & Hashimoto, H. (2004). A continuous satellite-derived measure of global terrestrial primary production. *BioScience*, *54*(6), 547–560. doi: 10.1641/0006-3568(2004)054[0547:ACSMOG]2.0.CO;2

Running, S. W., & Zhao, M. (2015). *User's Guide Daily GPP and Annual NPP (MOD17A2/A3) Products NASA Earth Observing System MODIS Land Algorithm* [Computer software manual].

Ryu, Y., Baldocchi, D. D., Ma, S., & Hehn, T. (2008). Interannual variability of evapotranspiration and energy exchange over an annual grassland in California. *Journal of Geophysical Research: Atmospheres*, *113*(D9). doi: 10.1029/2007JD009263

Schmit, T. J., & Gunshor, M. M. (2020). ABI Imagery from the GOES-R Series. In *The GOES-R Series* (pp. 23–34). Elsevier. doi: 10.1016/B978-0-12-814327-8.00004-4

Schulze, E.-D., & Hall, A. E. (1982). Stomatal Responses, Water Loss and CO_2

Assimilation Rates of Plants in Contrasting Environments. In O. L. Lange, P. S. Nobel, C. B. Osmond, & H. Ziegler (Eds.), *Physiological Plant Ecology II: Water Relations and Carbon Assimilation* (pp. 181–230). Berlin, Heidelberg: Springer. doi: 10.1007/978-3-642-68150-9_8

Seabold, S., & Perktold, J. (2010). statsmodels: Econometric and statistical modeling with python. In *9th python in science conference.*

Sims, D. A., Brzostek, E. R., Rahman, A. F., Dragoni, D., & Phillips, R. P. (2014). An improved approach for remotely sensing water stress impacts on forest c uptake. *Global Change Biology*, *20*(9), 2856–2866. doi: https://doi.org/10.1111/gcb.12537

Stocker, B. D., Zscheischler, J., Keenan, T. F., Prentice, I. C., Seneviratne, S. I., & Peñuelas, J. (2019). Drought impacts on terrestrial primary production underestimated by satellite monitoring. *Nature Geoscience*, *12*(4), 264–270. doi: 10.1038/s41561-019-0318-6

Stoy, P. C., Katul, G. G., Siqueira, M. B., Juang, J.-Y., Novick, K. A., Uebelherr, J. M., & Oren, R. (2006). An evaluation of models for partitioning eddy covariance-measured net ecosystem exchange into photosynthesis and respiration. *Agricultural and Forest Meteorology*, *141*(1), 2–18. doi: 10.1016/j.agrformet.2006.09.001

Stoy, P. C., Katul, G. G., Siqueira, M. B. S., Juang, J.-Y., McCarthy, H. R., Kim, H.-S., ... Oren, R. (2005). Variability in net ecosystem exchange from hourly to inter-annual time scales at adjacent pine and hardwood forests: a wavelet analysis. *Tree Physiology*, *25*(7). doi: 10.1093/treephys/25.7.887

Tang, J., Baldocchi, D. D., & Xu, L. (2005). Tree photosynthesis modulates soil respiration on a diurnal time scale. *Global Change Biology*, *11*(8), 1298–1304. doi: https://doi.org/10.1111/j.1365-2486.2005.00978.x

Thimijan, R., & Heins, R. (1983). Photometric, radiometric, and quantum light units of measure: a review of procedures for interconversion. *Hortic Sci*, *18*, 818–822.

Tuzet, A., Perrier, A., & Leuning, R. (2003). A coupled model of stomatal conductance, photosynthesis and transpiration. *Plant, Cell & Environment*, *26*(7), 1097–1116. doi: 10.1046/j.1365-3040.2003.01035.x

Virtanen, P., Gommers, R., Oliphant, T. E., Haberland, M., Reddy, T., Cournapeau, D., ... SciPy 1.0 Contributors (2020). SciPy 1.0: Fundamental Algorithms for Scientific Computing in Python. *Nature Methods*, *17*, 261–272. doi: 10.1038/s41592-019-0686-2

Wanner, W., Li, X., & Strahler, A. H. (1995). On the derivation of kernels for kernel-driven models of bidirectional reflectance. *Journal of Geophysical Research: Atmospheres*, *100*, 21077–21089. doi: 10.1029/95JD02371

Weiss, A., & Norman, J. (1985). Partitioning solar radiation into direct and diffuse, visible and near-infrared components. *Agricultural and Forest Meteorology*, *34*(2), 205–213. doi: 10.1016/0168-1923(85)90020-6

Wilson, K. B., Baldocchi, D., Falge, E., Aubinet, M., Berbigier, P., Bernhofer, C., ... Wofsy, S. (2003). Diurnal centroid of ecosystem energy and carbon fluxes at FLUXNET sites. *Journal of Geophysical Research: Atmospheres*, *108*. doi: https://doi.org/10.1029/2001JD001349

Wilson, R. (2013). Py6s: A python interface to the 6s radiative transfer model. *Computers & Geosciences*, *51*, 166–171. doi: 10.1016/j.cageo.2012.08.002

Wu, G., Guan, K., Jiang, C., Peng, B., Kimm, H., Chen, M., ... Cendrero-Mateo, M. P. (2020). Radiance-based NIRv as a proxy for GPP of corn and soybean. *Environmental Research Letters*, *15*(3), 034009. doi: 10.1088/1748-9326/ab65cc

Wutzler, T., Lucas-Moffat, A., Migliavacca, M., Knauer, J., Sickel, K., Šigut, L., ... Reichstein, M. (2018). Basic and extensible post-processing of eddy covariance flux data with REddyProc. *Biogeosciences*, *15*(16), 5015–5030. doi:

10.5194/bg-15-5015-2018

Xiao, J., Chevallier, F., Gomez, C., Guanter, L., Hicke, J. A., Huete, A. R., ... Zhang, X. (2019). Remote sensing of the terrestrial carbon cycle: A review of advances over 50 years. *Remote Sensing of Environment*, *233*, 111383. doi: 10.1016/j.rse.2019.111383

Xiao, J., Fisher, J. B., Hashimoto, H., Ichii, K., & Parazoo, N. C. (2021). Emerging satellite observations for diurnal cycling of ecosystem processes. *Nature Plants*. doi: 10.1038/s41477-021-00952-8

Xu, L., & Baldocchi, D. D. (2003). Seasonal trends in photosynthetic parameters and stomatal conductance of blue oak (Quercus douglasii) under prolonged summer drought and high temperature. *Tree Physiology*, *23*(13), 865–877. doi: 10.1093/treephys/23.13.865

Yuan, W., Cai, W., Xia, J., Chen, J., Liu, S., Dong, W., ... Wohlfahrt, G. (2014). Global comparison of light use efficiency models for simulating terrestrial vegetation gross primary production based on the LaThuile database. *Agricultural and Forest Meteorology*, *192-193*, 108–120. doi: 10.1016/j.agrformet.2014.03.007

Yuan, W., Liu, S., Zhou, G., Zhou, G., Tieszen, L. L., Baldocchi, D., ... Wofsy, S. C. (2007). Deriving a light use efficiency model from eddy covariance flux data for predicting daily gross primary production across biomes. *Agricultural and Forest Meteorology*, *143*(3), 189–207. doi: 10.1016/j.agrformet.2006.12.001

Zhang, Y., Xiao, X., Guanter, L., Zhou, S., Ciais, P., Joiner, J., ... Stocker, B. D. (2016). Precipitation and carbon-water coupling jointly control the interannual variability of global land gross primary production. *Scientific Reports*, *6*(1), 39748. doi: 10.1038/srep39748

Zhang, Y., Xiao, X., Zhang, Y., Wolf, S., Zhou, S., Joiner, J., ... de Grandcourt, A. (2018). On the relationship between sub-daily instantaneous and daily total gross primary production: Implications for interpreting satellite-based SIF retrievals. *Remote Sensing of Environment*, *205*, 276–289. doi: 10.1016/j.rse.2017.12.009

Zscheischler, J., Mahecha, M. D., von Buttlar, J., Harmeling, S., Jung, M., Rammig, A., ... Reichstein, M. (2014). A few extreme events dominate global interannual variability in gross primary production. *Environmental Research Letters*, *9*(3), 035001. doi: 10.1088/1748-9326/9/3/035001